Electric Energy During Magnetogenesis from Reheating

Nousaba Nasrin Protiti

September 27, 2023

Supervised by

Axel Brandenburg

Professor, NORDITA

Abstract

The process of converting electromagnetic energy into magnetohydrodynamic energy is crucial during the reheating phase in the early universe, occurring at the end of inflation and before the radiation-dominated era emerges. Our objective is to look at some toy model about how energies are converted from electromagnetic energy into magnetohydrodynamic energy when the universe goes from low conductivity to a high conductivity medium. The findings from our study reveal that the primary source of conversion into kinetic and thermal energies is the dissipation of electric energy, with magnetic energy playing a secondary role in this transformation. This implies that, since electric energy is dominant over magnetic energy during inflation and reheating, substantial amounts of electric energy can be efficiently converted into magnetohydrodynamic energy when conductivity becomes significant before the corresponding length scales enter the horizon and stabilize.

The material presented in this thesis has been presented in the following paper:

Contents

List of Figures

List of Tables

1 Introduction

In our present universe, magnetic fields undergo a constant process of regeneration through dynamo mechanisms, operating at scales ranging from individual galaxies to large galaxy clusters. This magnetic field rejuvenation primarily draws its energy from gravitational forces, which manifest through processes like accretion or direct collapse. It is worth noting that magnetic fields may also extend to even larger spatial scales. However, according to Durrer and Neronov 2013 and Subramanian 2016, when we venture into the spaces between galaxy clusters, often referred to as cosmic voids, the conventional wisdom suggests that generating magnetic fields through contemporary dynamo action becomes exceedingly challenging. Nevertheless, we have indirect evidence pointing to the existence of magnetic fields in these cosmic voids. Specifically, we have lower limits on magnetic field strength derived from observations of halos surrounding blazars, which are active galactic nuclei emitting TeV photons. These high-energy photons interact with the extragalactic background light via inverse Compton scattering, producing GeV photons as a result. Interestingly, we don't observe these secondary GeV photons. One plausible explanation is the presence of an intervening magnetic field, estimated to be around 10^{-16} Gauss, spread over a megaparsec scale (Neronov and Vovk 2010 and Taylor, Vovk, and Neronov 2011). It is also worth noting that there could be other factors contributing to the non-observation of GeV photons, such as plasma instabilities, which may interfere with the electron-positron beam (Broderick, Chang, and Pfrommer 2012 and Broderick, Tiede, et al. 2018). However, even in such scenarios, a portion of the disruption in the plasma beam might still be attributed to the presence of magnetic fields (Sironi and Giannios 2014). This could potentially provide an explanation for the GeV halos seen around at least some blazars (Batista, Saveliev, and Gouveia Dal Pino 2019). If indeed magnetic fields exist on truly cosmic scales, they might have originated in the primordial phases of the universe. This implies that they could have been created during or prior to the radiation-dominated era of the universe, perhaps during one of the cosmological phase transitions or even during the inflationary period. Notably, inflation is a phase where the conversion from electromagnetic fields to magnetohydrodynamic fields played a significant role, which is our topic of interest.

The end of reheating in the early universe refers to a crucial period after cosmic inflation, a hypothetical rapid expansion that occurred shortly after the Big Bang. According to the theory of inflation, the universe experienced exponential growth, stretching out its fabric and smoothing out irregularities.

According to the theory of inflation, the universe was dominated by an inflaton field—a scalar field responsible for driving inflation. As inflation ended, the inflaton field began to oscillate around the minimum of its potential energy. During these oscillations, the energy of the inflaton field is gradually converted into other particles, a process known as reheating.

Reheating is a significant phase in the early universe because it marks the transition from the inflationary phase to a radiation-dominated phase, setting the stage for the subsequent evolution of the universe. The energy transfer during reheating leads to the production of particles, such as photons, electrons, quarks, and other elementary particles, which eventually

form the building blocks of matter.

The precise details of the reheating process depend on the specific particle physics model that describes the inflaton field and its interactions. In some models, reheating is primarily driven by the decay of the inflaton field into other particles Kofman, Linde, and Starobinsky 1994. The inflaton field's decay can be a rapid or gradual process, leading to different reheating scenarios (Ahmed, Grzadkowski, and Socha 2022).

The end of reheating occurs when the energy transfer from the inflaton field to other particles is complete, and the universe becomes radiation-dominated. At this point, the energy density of the universe is dominated by the thermal radiation produced during reheating. The temperature of the universe is determined by the energy of these thermalized particles and sets the starting conditions for subsequent cosmological epochs, such as Big Bang nucleosynthesis and the formation of the cosmic microwave background radiation.

Understanding the end of reheating is crucial for cosmology as it connects the physics of inflation, particle physics, and the early universe. The precise mechanisms and timescales of reheating are still subjects of active research and depend on the details of the underlying particle physics model. The study of reheating provides insights into the fundamental processes that shaped the early universe and its subsequent evolution.

2 Theory

2.1 Magnetogenesis: Inflation and reheating

Magnetogenesis is a fascinating and complex field within cosmology that seeks to explain the generation of magnetic fields in the early Universe. These magnetic fields are thought to have played a crucial role in the evolution of cosmic structures, galaxies, and even in the formation of our Milky Way galaxy. One of the intriguing aspects of magnetogenesis is its connection to inflation and reheating, which are pivotal processes in the early Universe's evolution.

Inflation is a theoretical concept proposed to explain the remarkable uniformity and flatness of the observable Universe. It posits that a rapid and exponential expansion of the Universe occurred in its early moments, smoothing out irregularities and setting the stage for the large-scale structure we observe today.

During this inflationary epoch, as discussed by Mukhanov, Feldman, and Brandenberger 1992, quantum fluctuations in the inflaton field are believed to have given rise to primordial perturbations, including density fluctuations and gravitational waves.

Reheating is the subsequent process following inflation when the Universe transitions from this inflationary phase to a radiation-dominated era. It involves the conversion of the energy stored in the inflaton field into other particles, such as radiation and matter, and marks the end of inflation.

Magnetogenesis during inflation and reheating is a theory that suggests that magnetic fields can be generated during these early cosmic epochs. One mechanism for this generation involves the coupling of the electromagnetic field to the inflaton field. Quantum fluctuations in the inflaton field can then induce fluctuations in the electromagnetic field, leading to the generation of primordial magnetic fields.

According to Brandenburg and Sharma 2021 there is a connection between inflation, magnetogenesis, and gravitational waves. Gravitational waves are ripples in spacetime predicted by Einstein's theory of General Relativity. They can be produced by various astrophysical processes, including the rapid expansion of the Universe during inflation. Their paper investigates how magnetogenesis during inflation could leave an imprint on the cosmic microwave background (CMB) and potentially generate relic gravitational waves. Detecting such gravitational waves would provide valuable insights into the early Universe's conditions, including the presence and strength of primordial magnetic fields.

It is important to note that magnetogenesis is a topic of ongoing research, and while it presents an intriguing connection between inflation, reheating, and the generation of magnetic fields, there is still much to be understood and confirmed in this field. Researchers continue to explore various mechanisms and conduct experiments, including observations of the CMB and gravitational waves, to test and refine our understanding of magnetogenesis and its role in the cosmic evolution.

In models of inflationary magnetogenesis, it is assumed that conformal invariance is broken through a coupling to a scalar field, often exemplified by the inflaton. It is worth noting that

an alternative coupling exists through an axion field, resulting in helical magnetogenesis, but we will not delve into that aspect here. The dynamics of the scalar field in this context are intriguing and can be found in Adshead, Jr., et al. 2015, Adshead, Giblin, Scully, et al. 2016 and Adshead, Giblin, Pieroni, et al. 2020. To simplify the model, it is common practice to replace this coupling with a prefactor denoted as f^2,' where f depends on the universe's scale factor. This f^2 factor plays a crucial role in the electromagnetic energy contribution to the Lagrangian density, expressed as $f^2 F^{\mu\nu} F_{\mu\nu}$ with $F_{\mu\nu}$ representing the Faraday tensor, as explained by Ratra 1992. Early approaches to inflationary magnetogenesis faced specific challenges, including the issues of strong coupling, backreaction problems as described by Demozzi, Mukhanov, and Rubinstein 2009, and constraints related to the Schwinger effect. The Schwinger effect can lead to an untimely surge in electric conductivity, short-circuiting the electric field and hindering further growth of the magnetic field (Kobayashi and Afshordi 2014). This concern is especially pertinent for models that address the backreaction problem by opting for low-energy scale inflation (Ferreira, Jain, and Sloth 2013). However, it could be mitigated if charged particles acquire sufficiently high masses through mechanisms in the early universe (Kobayashi and Sloth 2019). These three issues can be circumvented by imposing certain constraints on the function f, as described by Sharma, Jagannathan, et al. 2017 and Sharma, Subramanian, and Seshadri 2018. For the specific purpose of discussing the conversion of electromagnetic energy, which is our primary focus, these models serve as a useful choice.

Three-dimensional simulations of inflationary magnetogenesis have been conducted by assuming a sudden transition from an electromagnetic regime devoid of currents to a magnetohydrodynamic regime where the displacement current is already disregarded (Brandenburg and Sharma 2021 and Brandenburg, He, and Sharma 2021). These simulations involve solving the evolution equations for the scaled magnetic vector potential, denoted as $\boldsymbol{\mathcal{A}} \equiv f \boldsymbol{A}$, within the Coulomb gauge (see, e.g., Subramanian 2010)

$$\left[\frac{1}{c^2} \frac{\partial^2}{\partial t^2} - \nabla^2 - k_*^2(t) \right] \boldsymbol{\mathcal{A}} = 0. \tag{1}$$

Here, $k_*^2(t) = f''/f$ is a generation term because it destabilizes the field at large length scales for wavenumbers $k < k_*(t)$. Analogous to the primes on $a(t)$, primes on $f(t)$ also denote conformal time derivatives. Toward the end of the reheating phase, where $f \to 1$, we expect $k_*(t) \to 0$. Our objective is to present calculations where the transition from a vacuum state to high conductivity is smooth and continuous. To determine the generation term $k_*(t)$, a commonly used approach is to employ a power-law representation in terms of $a(t)$. Specifically, during inflation, f follows $f \propto a^\alpha$ with $\alpha > 0$ while during reheating, it follows $f \propto a^{-\beta}$ with $\beta > 0$ (Subramanian 2010). We focus on the reheating phase, where $a(t) \propto t^2$ (Sharma, Jagannathan, et al. 2017 and Sharma, Subramanian, and Seshadri 2018) making f equal to 1 when the radiation-dominated era begins, and thus $f = 1$ and $k_*^2(t) = 0$ for $a > 1$. For $a < 1$ however, we have,

$$k_*^2(t) = \beta \left[(\beta + 1)(a'/a)^2 - a''/a \right]. \tag{2}$$

It is important to note that for $a = t^2$, we have $a' = 2t$ and $a'' = 2$, so $(a'/a)^2 = 4/t^2$ and $a''/a = 2/t^2$, and therefore, $f''/f = 2\beta(2\beta + 1)/t^2$. In contrast to previous numerical work Brandenburg and Sharma 2021 and Brandenburg, He, and Sharma 2021 the inclusion of the displacement current is now maintained consistently throughout. However, a challenge arises as $k_*(t)$ exhibits a discontinuity, transitioning from $k_*^2(1) = \beta(\beta + 1) \neq 0$ to zero at the moment when conductivity is activated. In the simulations, this discontinuity did not appear to significantly affect the results, as the magnetic field at the end of the electromagnetic phase merely served as an initial condition for the magnetohydrodynamic calculations after the transition. Nevertheless, in a continuous calculation without such a switch, this issue must be addressed.

2.2 Conformal time: Cosmological expansion scaled out

Conformal time is a used in cosmology and relativistic physics to describe the progression of time in a way that accounts for the expansion of the Universe. It is a coordinate system that scales out the effects of cosmic expansion, making it a useful tool for simplifying the equations of General Relativity and understanding the evolution of the Universe.

In cosmology, the expansion of the Universe is a fundamental phenomenon described by Hubble's law, which states that galaxies are receding from each other, and the rate of recession is proportional to their distance. This expansion affects not only the spatial dimensions of the Universe but also the passage of time itself.

Now, to get the conformal time η, we need to solve the equation

$$dt_{\mathrm{conf}} = \frac{dt_{\mathrm{phys}}}{a(t)}. \tag{3}$$

So, conformal time can be defined as

$$t_{\mathrm{conf}} = \int \frac{dt_{\mathrm{phys}}}{a(t)}. \tag{4}$$

In this equation, t_{phys} is the proper time, which is the time experienced by an observer at a particular location in the Universe; and a is the scale factor of the Universe as a function of cosmic or conformal time. The scale factor represents the relative size of the Universe at different times.

In the following, however, we always work with conformal time and therefore drop the subscript from now on.

2.3 Dominance of electric energy over magnetic energy

In the early universe, during the first moments after the Big Bang (at extremely high energies and temperatures) the behavior of electromagnetic forces, specifically the electric and magnetic fields, can differ significantly from what we experience today. In standard hydrodynamic turbulence, energy dissipation equals the energy input via forcing. However, the presence of

magnetic fields introduces additional complexity. Energy can be transferred from kinetic to magnetic energy, working against the Lorentz force. This leads to a situation with two exit channels, making it unclear which dominates in specific scenarios. This can be further explained using a reversed dynamo, where at large conductivities, magnetic energy can convert back into kinetic energy at smaller length scales. Brandenburg and Protiti 2023 focused on the transition of electric conductivity from zero (vacuum) to high values.

In the scenario where reheating is initiated by the feedback stemming from the Schwinger effect, we would witness a supply of thermal energy from both ϵ_{K} and ϵ_{M}. Consequently, this would establish a direct connection between the ensuing heating process and the emergence of the parameter σ. This intricate interplay of energy transfer between the magnetic, electric, and kinetic energy reservoirs is thoughtfully depicted in Figure 1
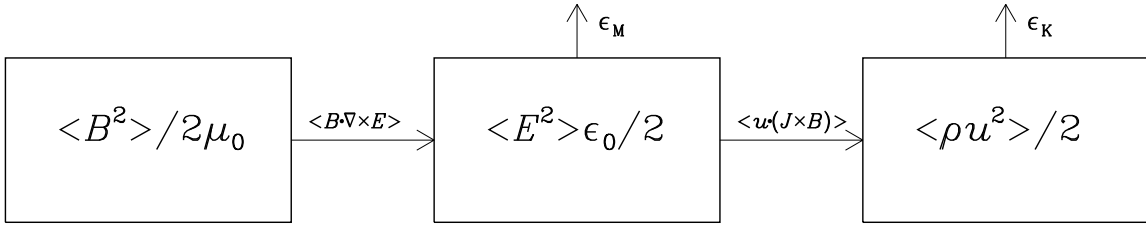
Figure 1: Energy conversion from magnetic to kinetic energies via the electric energy reservoir.

β	$2\beta+1$	$2\beta+1/2$	$k_*(1)$
1	3	2.5	2.45
2	5	4.5	4.47
4	9	8.5	8.49

Table 1: Parameters relevant for the models with different values of β.

The wavenumber below which the solution is still unstable, is determined by the generation term $k_*^2(t) \equiv f''/f$. Table 1 shows that $ctk = \mathrm{const} \approx 2\beta + 1/2$ due to the fact that $k_*^2(t) = 2\beta(2\beta+1)/t^2$; see Equation (2) and the application to the end of reheating below that equation.

It is easy to see that on large length scales, when the ∇^2 operator in Equation (1) is negligible compared with $k_*^2(t)$, we have

$$\mathcal{A}_z(x,t) = A_0 t^{2\beta+1} k^{-1} \cos kx, \tag{5}$$

$$A_z(x,t) = \mathcal{A}_z/f = A_0 t^{\beta+1} k^{-1} \cos kx, \tag{6}$$

$$B_y(x,t) = A_0 t^{\beta+1} \sin kx, \tag{7}$$

$$E_z(x,t) = -\partial A_z/\partial t = -(\beta+1)A_0 t^\beta k^{-1} \cos kx. \tag{8}$$

For $ckt \gtrsim 1$, which corresponds to the super-horizon scales, where the modes are still in an unstable state, we observe that $tE_{\mathrm{rms}}/B_{\mathrm{rms}} \approx \beta + 1$. As we move to smaller length scales,

i.e., for larger values of k, the modes stabilize, and we encounter the familiar behavior of electromagnetic waves.

We still need to decide when we would start modeling the transition from a vacuum to one of high conductivity and the related Joule heating, i.e., we need to set values of t_0 and t_{trans}. We obtain solutions where electromagnetic waves have already been established if we choose a value of t_0 that is too large.

3 Methods

3.1 The PENCIL CODE

The Pencil Code refers to a specific software package or framework used for simulating MHD phenomena using computational methods. It is designed to solve the MHD equations numerically and simulate the behavior of plasmas in the presence of magnetic fields.

This type of code is useful for understanding complex phenomena like solar flares, magnetic reconnection, and the behavior of plasmas in fusion reactors Collaboration et al. 2021. In this study, we employed the Pencil Code, a versatile computational tool widely used for simulating magnetohydrodynamic (MHD) phenomena.

The PENCIL CODE is a finite-difference code primarily designed to solve the compressible MHD equations in a three-dimensional Cartesian grid. It incorporates high-order numerical schemes for accurate and efficient simulations of fluid dynamics in the presence of magnetic fields. The code utilizes MPI (Message Passing Interface) for parallel processing, enabling efficient computation on distributed systems. Its modular design allows researchers to easily add or modify components to suit different problem domains, making it versatile for various scientific simulations. Collaboration et al. 2021 The MHD equations, which describe the evolution of fluid density, velocity, pressure, and magnetic field, were numerically solved using the Pencil Code. Spatial derivatives are calculated using central finite differences, ensuring accurate representation of gradients even for complex flows. Time integration is achieved through explicit time-stepping methods, with the Courant-Friedrichs-Lewy (CFL) condition used to determine the time step size. To simulate physical systems in bounded domains, appropriate boundary conditions can be imposed on the simulation domain. These included reflective, periodic, and outflow conditions, depending on the specific scenario being modeled. Careful consideration was given to the choice of boundary conditions to minimize artificial effects and ensure accurate representation of the physics. Key simulation parameters, such as domain size, resolution, initial conditions, and magnetic field strength, were carefully chosen based on the specific scientific questions under investigation.

3.2 Governing equations

In the post-inflationary era, the MHD equations can be derived from Maxwell's equations, which state the fundamentals of electricity and magnetism.

$$\boldsymbol{\nabla} \cdot \boldsymbol{E} = \rho_{\mathrm{e}}/\epsilon_0 \qquad [\text{Gauss's law}] \tag{9}$$

$$\boldsymbol{\nabla} \cdot \boldsymbol{B} = 0 \qquad [\text{Gauss's law for magnetism}] \tag{10}$$

$$\boldsymbol{\nabla} \times \boldsymbol{E} = -\frac{\partial \boldsymbol{B}}{\partial t} \qquad [\text{Faraday's law of induction}] \tag{11}$$

$$\boldsymbol{\nabla} \times \boldsymbol{B} = \mu_0 \boldsymbol{J} + \frac{1}{c^2}\frac{\partial \boldsymbol{E}}{\partial t} \qquad [\text{Ampere's law}] \tag{12}$$

The symbols used here can be defined as following,

E is the electric field

B is the magnetic field

J is the current density

μ_0 is the vacuum permeability

c is the speed of light

We begin by studying here a simple one-dimensional model, where an electromagnetic wave with equal amounts of electric and magnetic energies gets converted into magnetic and kinetic energies as the conductivity increases and the electric field short-circuits. In one-dimension the divergence equations (Equation (9) and Equation (10)) vanishes and the only remaining equations (Equation (11) and Equation (12)) are the curl of electric and magnetic fields, which represent their evolution with time.

The evolution of the electric and magnetic fields, E and B, respectively, is given by the Maxwell equations, written here in SI units:

$$\frac{1}{c^2}\frac{\partial E}{\partial t} = \nabla \times B - \mu_0 J, \tag{13}$$

$$\frac{\partial B}{\partial t} = -\nabla \times E, \tag{14}$$

where c is the speed of light and μ_0 is the vacuum permeability. Equation (13) implies the generation of charge To close the equations, we use Ohm's law,

$$J = \sigma\left(E + u \times B\right), \tag{15}$$

where σ is the electric conductivity and u is the velocity. Usually Ohm's law tells us how the current density is related to the force acting on free charges in a medium and is given by, $J = \sigma E$; see Davidson 2016. But in MHD, we also need to consider the electric field in a co-moving frame with the velocity of the plasma, which leads to the form Equation (15).

In the early universe, during the inflationary period, the plasma is highly diluted, leading to a state where there are virtually no particles present. Consequently, the electric conductivity of the universe becomes extremely low, approaching zero. However, as the universe evolves, a phase of reheating becomes necessary. One proposed mechanism for this reheating phase is related to the stretching caused by the cosmological expansion. This expansion leads to the amplification of electromagnetic fields until the electric field strength surpasses a critical value, known as the Schwinger effect threshold.

Kobayashi and Afshordi 2014 showed that, when this threshold is exceeded, it triggers the production of charged particles, resulting in the emergence of electric conductivity in the universe. This transition in the electric conductivity (denoted as σ) suggests the existence of an

intermediate phase where σ takes on a specific value for a certain duration. During this phase, there is an associated electromagnetic energy loss, quantified as the dot product of the current density ($\boldsymbol{J}$) and the electric field ($\boldsymbol{E}$). This process is a well-established phenomenon in the field of magnetohydrodynamics, where the displacement current is disregarded. In magnetohydrodynamics, the equations that describe the relationship between magnetic energy and other physical properties are used to derive the magnetic energy equation. Ignoring the displacement current we have,

$$\frac{\partial}{\partial t}\left(\boldsymbol{B}^2/2\mu_0\right) = -\boldsymbol{B}\cdot\boldsymbol{\nabla}\times\boldsymbol{E}/\mu_0 = \boldsymbol{J}\cdot\boldsymbol{E} - \boldsymbol{\nabla}\cdot(\boldsymbol{E}\times\boldsymbol{B}/\mu_0), \tag{16}$$

where $\boldsymbol{E}\times\boldsymbol{B}/\mu_0$ is the Poynting vector. Introducing volume average, which we denote with angle brackets,

$$\frac{\mathrm{d}}{\mathrm{d}t}\left\langle\boldsymbol{B}^2/2\mu_0\right\rangle = -\left\langle\boldsymbol{J}\cdot\boldsymbol{E}\right\rangle. \tag{17}$$

Using Ohm's law we get,

$$\left\langle\boldsymbol{J}\cdot\boldsymbol{E}\right\rangle = \left\langle\boldsymbol{J}^2/\sigma\right\rangle + \left\langle\boldsymbol{u}\cdot(\boldsymbol{J}\times\boldsymbol{B})\right\rangle = \epsilon_\mathrm{M} + W_\mathrm{L} \tag{18}$$

The flows of energy between magnetic, electric, and kinetic energy reservoirs is illustrated in Figure 1. We denote those as

$$\mathcal{E}_\mathrm{M} \equiv \langle\boldsymbol{B}^2/2\mu_0\rangle, \quad \mathcal{E}_\mathrm{E} \equiv \langle\epsilon_0\boldsymbol{E}^2/2\rangle, \quad \text{and} \quad \mathcal{E}_\mathrm{K} \equiv \langle\rho\boldsymbol{u}^2/2\rangle, \tag{19}$$

respectively.

The momentum and continuity equations,

$$\rho\frac{\mathrm{D}\boldsymbol{u}}{\mathrm{D}t} = -\boldsymbol{\nabla}p + \boldsymbol{J}\times\boldsymbol{B} + \boldsymbol{\nabla}\cdot(2\rho\nu\mathsf{S}), \tag{20}$$

$$\frac{\mathrm{D}\ln\rho}{\mathrm{D}t} = -\boldsymbol{\nabla}\cdot\boldsymbol{u}, \tag{21}$$

where $\mathrm{D}/\mathrm{D}t \equiv \partial/\partial t + \boldsymbol{u}\cdot\boldsymbol{\nabla}$ is the advective derivative, $p = \rho c_\mathrm{s}^2$ is the pressure for an isothermal equation of state with sound speed c_s, which is constant, ν is the viscosity, and $\mathsf{S}_{ij} = (\partial_i u_j + \partial_j u_i)/2 - \delta_{ij}\boldsymbol{\nabla}\cdot\boldsymbol{u}/3$ are the components of the rate-of-strain tensor S.

3.3 The displacement current module

Faraday's law (Equation (13)) and the induction equation (Equation (14)) or its uncurled version (in the Weyl gauge, i.e., without the electrostatic potential),

$$\frac{\partial\boldsymbol{A}}{\partial t} = -\boldsymbol{E}, \tag{22}$$

needs to be solved as the displacement current can not be neglected in electromagnetism. For this the module named 'disp_current' was used. The module is structured with subroutines to

initialize, calculate, and manipulate various quantities related to electric fields, vector potentials, and magnetic fields. The main components are:

1. Imports and input parameters: It imports several other modules and subroutines for necessary functionalities. The module defines various input parameters such as amplitudes, wavenumbers, phases of the three components of the electric field, and other settings that control the behavior of the electromagnetic fields in the simulation. One example for this is the speed of light which is squared as input parameter, so it is usually not computed self-consistently from the actual speed of light.

2. Subroutines and functions:

   - register_special configures and registers the electric field that is used within the module

   - initialize_special initializes module variables based on input parameters

   - init_special sets initial conditions for the electric field (see below)

   - pencil_criteria_special specifies pencils (spatial regions) of the simulation that are relevant for this module. In particular, the current density, from Equation 15, which is computed in `magnetic.f90`, must be requested

   - calc_pencils_special calculates the values of certain variables (pencils) based on the current state of the simulation. These include pencils for the vector $\boldsymbol{E}$, the quantity $\boldsymbol{E}^2$, $\boldsymbol{E} \cdot \boldsymbol{\nabla} \boldsymbol{B}$ and $\boldsymbol{B} \cdot \boldsymbol{\nabla} \boldsymbol{E}$ that are used for diagnostic purposes

   - dspecial_dt calculates the right-hand side of differential equations that govern the evolution of the electromagnetic fields over time (Equation (13),Equation (14))

   - read_special_init_pars and write_special_init_pars read and write input parameters from and to a file

   - read_special_run_pars and write_special_run_pars read and write run-time parameters from and to a file

   - rprint_special manages printing and reporting of diagnostic and analysis information

   - get_slices_special generates slices of $\boldsymbol{E}$ for visualization

3. Use of other modules: The module uses other modules. These modules which provide functionalities related to parallel computing, data manipulation, diagnostics, and more. One of the modules used here is 'cparam' which is mentioned below.

3.4 The magnetic field module

This modules deals with all aspects of magnetic fields and includes declarations, parameters, and variables related to magnetic field calculations and simulations; assuming there is an imposed magnetic fields. The key elements of this module are:

1. Use of other modules: The module also uses some other modules such as 'cparam' which is mentioned before.

2. Variable declarations: The module declares a range of real and integer variables that hold various physical parameters, constants, and computational settings. These parameters control the behavior of the magnetic field calculations and simulations. They are also defined and initialized later.

3. Logical flags: There are numerous logical flags (variables with boolean values - true/false) that control the execution of specific parts of the code. These flags determine which routines and calculations are enabled or disabled based on simulation requirements.

4. Array declarations: The module declares arrays with dimensions that are likely related to spatial grids used in the simulations. For instance, there are arrays like bb_xy, jj_xy, aps_xy, aamz, etc.

5. Diagnostic quantities: Each diagnostic variable corresponds to a specific quantity that the simulation aims to analyze or measure. These quantities are related to various aspects of the plasma or MHD system being simulated. For example:

   - idiag_eta_tdep represents the time-dependent resistivity (η) in the simulation

   - idiag_ab_int represents the volume integral of the dot product of vector $\boldsymbol{A}$ and vector $\boldsymbol{B}$

   - idiag_jb_int represents the volume integral of the dot product of current density $\mathbf{j}$ and vector $\boldsymbol{B}$

   - xyaver.in associated with quantities that have been averaged over the x-y plane

   - xzaver.in related to quantities that have been averaged over the x-z plane

   - yzaver.in associated with quantities that have been averaged over the y-z plane

   - yaver.in associated with quantities that have been averaged over the y-direction

   - zaver.in related to quantities that have been averaged over the z-direction, etc. Some other variables are also mentioned here which are related to vector potential (aa), electric field (ee), magnetic field (bb), current density (jj), resistivity (eta), Alfven speed (alfven), and other quantities associated with MHD simulations.

6. Precalculations: Some precalculations are done, such as calculating the inverse of the inertial length squared (linertial_2) and the inverse of the nu_ni coefficient (nu_ni1).

7. Calculation of B-field related values: The code calculates various values related to the external magnetic field (B_ext), such as its magnitude squared (B_ext2), its inverse squared magnitude (B_ext21), unit vector (B1_ext), and a vector (B_ext_inv) used in calculations. For each specified method in the 'initaa' array, there is a subroutine that calculates and sets the magnetic field values in the f array.

8. Mathematical operations: Various mathematical operations are performed to calculate the magnetic field values. These operations involve trigonometric functions (sin, cos), hyperbolic functions (tanh), exponential functions, etc. These calculations are used to define the structure of the magnetic field based on the chosen initialization method.

9. Error handling: The module also includes error checks and fatal error calls in certain cases to handle unexpected conditions.

3.5 Suitable initial conditions

The initial conditions chosen for magnetic and electric energy spectra during the matter-dominated era in the post-inflation universe play

an important role in the numerical simulations and also in understanding how the magnetic and electric energy spectra evolve during the matter-dominated era. In the post-inflation matter-dominated era, the magnetic field spectrum is initially scale invariant during inflation but does not contribute significantly to the growing solution in this era.

However, there is a contribution proportional to k^3 for the scales of interest. As a result, for super-Hubble scales, only the k^3 spectrum is present, as discussed by Sharma, Jagannathan, et al. 2017 and Brandenburg and Sharma 2021.

In one dimension with $\partial/\partial x \neq 0$ and $\sigma = 0$, we can have electromagnetic waves, for example, $B_y^\pm(x, t) = B_{y0} \sin k(x \mp ct)$ and $E_z^\pm(x, t) = \mp k B_{y0} \sin k(x \mp ct)$, traveling in the positive (negative) x direction. Note that the electric and magnetic energies are here equal to each other.

In the code, we use the initial condition `initaa='coswave-phase'` with `ampl_az=+.1` and `kx_az=1`, which means that $A_z = 0.1 \cos kx$. This implies that $B_y = 0.1 \sin kx$ and corresponds to the desired electromagnetic wave, $B_y^\pm(x, t) = B_{y0} \sin k(x \mp ct)$, for the upper sign with $B_{y0} = 0.1$, $k = 1$, and $c = 1$. Thus, our expression for $A_z^\pm$ can be written as

$$A_z^\pm = \frac{B_{y0}}{k} \cos k(x \mp ct). \tag{23}$$

This expression obeys Equation (22), i.e.,

$$E_z^\pm = -\frac{\partial A_z}{\partial t} = \mp c B_{y0} \sin k(x \mp ct). \tag{24}$$

To realize this in the code, we use for the electric field the initial condition `initee='coswave-phase'` with `ampl_ez=+.1`, `kx_ez=1`, and `phase_ez=1.5707963` ($\approx \pi/2$), which means that $E_z = 0.1 \sin kx$.

Once conductivity has emerged, the electromagnetic waves become replaced by Alfvén waves, provided we add a constant magnetic field B_{x0} in the x direction. Such a constant field does not change the electromagnetic waves. However, the propagation speed now changes

from c to the Alfvén speed $v_A = B_{x0}/\sqrt{\rho_0 \mu_0}$. Thus, instead of Equation (23), we now have

$$A_z^\pm = \frac{B_{y0}}{k} \cos k(x \mp v_A t). \tag{25}$$

Furthermore, Equation (24) becomes modified and now reads

$$E_z^\pm = -\frac{\partial A_z}{\partial t} = \mp v_A B_{y0} \sin k(x \mp v_A t). \tag{26}$$

In that case, however, the electric field is no longer controlled by the displacement current, but by Ohm's law, Equation (15), which, using perfect conductivity, $\sigma \to \infty$, implies $\boldsymbol{E} = -\boldsymbol{u} \times \boldsymbol{B}$, or $E_z^\pm = u_y^\pm B_{x0}$. Therefore, we have

$$u_y^\pm = \mp v_A \frac{B_{y0}}{B_{x0}} \sin k(x \mp v_A t). \tag{27}$$

This expression obeys the momentum equation (20), of which the relevant part is

$$\rho_0 \frac{\partial u_y^\pm}{\partial t} = J_z^\pm B_{x0}. \tag{28}$$

Here, $J_z^\pm = k^2 A_z^\pm$ is the current density in terms of $A_z^\pm$. Inserting the expressions above, we see that $\rho_0 k v_A^2 (B_{y0}/B_{x0}) \cos k(x \mp v_A t) = \mu_0^{-1} k B_{x0} B_{y0} \cos k(x \mp v_A t)$, which is evidently obeyed when using $v_A = B_{x0}/\sqrt{\rho_0 \mu_0}$.

3.6 The global parameters

The module 'cparam' contains various global parameters (constants) used throughout the program. It defines a range of constants and parameters for numerical simulations, computational grids, physical constants, and more. The main parts are:

1. Grid parameters that are related to the computational grid used in the simulation, such as grid dimensions (nx, ny, nz), total grid size (nxygrid, nxzgrid, nyzgrid), and the number of processors (nprocxy, nprocyz, nprocxz) in different directions. For the one-dimensional case, we have $nx = 128$, $ny = nz = 1$.

2. Derived and fixed parameters such as the total number of variables (mfarray), communication arrays (mcom), and parameters for different data structures. Two derived types are defined here: slice_data to hold slice information and boundary_condition to define module-specific boundary conditions.

3. Array dimensions that defines dimensions and indices for various arrays used in the simulation and includes definitions for array sizes (mx, my, mz, mxgrid, etc.), along with indexing ranges (l1, l2, m1, m2, etc.).

4. Yin-Yang Grid constants which are related to the Yin-Yang grid, a method used in spherical coordinate simulations.

For our simulations, we utilize the magnetic vector potential $\boldsymbol{A}$, to ensure that the magnetic field $\boldsymbol{B} = \boldsymbol{\nabla} \times \boldsymbol{A}$ maintains divergence-free properties. The evolution equation for $\boldsymbol{A}$ in this framework is expressed as:

$$\frac{1}{c^2}\frac{\partial^2 \boldsymbol{A}}{\partial t^2} - \nabla^2 \boldsymbol{A} + \boldsymbol{\nabla}\boldsymbol{\nabla}\cdot\boldsymbol{A} + \frac{1}{\eta(t)}\left(\frac{\partial\boldsymbol{A}}{\partial t} + \boldsymbol{u}\times\boldsymbol{B}\right) = 0, \tag{29}$$

where $\boldsymbol{\nabla}\cdot\boldsymbol{A} = 0$ holds when utilizing the Coulomb gauge. This equation shows that, when $\sigma \to 0$ or $\eta \to \infty$, we just have electromagnetic waves described by the wave equation $\ddot{\boldsymbol{A}} - c^2\nabla^2\boldsymbol{A} = 0$. In the opposite limit of $\sigma \to \infty$ or $\eta \to 0$, we obtained the usual uncurled induction equation where $\eta\nabla^2\boldsymbol{A}$ acts as a diffusion term.

Since the speed of light is now the fastest speed in the system, the time step is governed by a CFL condition where the speed of light enters, i.e., the time step Δt is never larger than $\Delta x/c$. Here, $\Delta x = L/N$ is the grid size in a periodic domain of size L represented by N mesh points.

4 Results

4.1 Energetics during emergence of conductivity

In the system depicted in Figure 1, there is no external energy input. However, this situation would alter if we were to introduce external forcing into the momentum equation (20). Furthermore, within our discussion, we delve into another possibility in greater depth, namely, the potential for energy injection during the reheating phase that marks the conclusion of the inflationary period.

Before discussing this in more detail, let us first discuss the energetics for the kinetic energy equation. By taking the dot product of Equation (20) with the velocity vector u, employing Equation (21), performing integration by parts, and considering the properties of $\partial_i u_j$ (which can be expressed as a sum of a symmetric and an antisymmetric tensor), we observe that when multiplied by S (a symmetric and trace-free tensor), there's no contribution when $\delta_{ij} \boldsymbol{\nabla} \cdot \boldsymbol{u}/3$ is added. Consequently, we find that $\mathsf{S}_{ij}\partial_i u_j = \mathsf{S}^2$, leading us to the evolution equation for kinetic energy in the following form:

$$\frac{\mathrm{d}}{\mathrm{d}t}\left\langle \rho \boldsymbol{u}^2/2 \right\rangle = -\left\langle \boldsymbol{u} \cdot \boldsymbol{\nabla}p \right\rangle + \left\langle \boldsymbol{u} \cdot (\boldsymbol{J} \times \boldsymbol{B}) \right\rangle - \left\langle 2\rho\nu\mathsf{S}^2 \right\rangle, \tag{30}$$

This equation can also be expressed more concisely as $\dot{\mathcal{E}}_{\mathrm{K}} = W_{\mathrm{P}} + W_{\mathrm{L}} - \epsilon_{\mathrm{K}}$, where $W_{\mathrm{P}} = -\langle \boldsymbol{u}\cdot\boldsymbol{\nabla}p \rangle$ is the work done by the pressure force, and $\epsilon_{\mathrm{K}} = \langle 2\rho\nu\mathsf{S}^2 \rangle$ represents viscous heating. The dot on the kinetic energy $\mathcal{E}_{\mathrm{K}}$ indicates a time derivative. It is important to note that the divergence term, $\boldsymbol{\nabla} \cdot (p\boldsymbol{u})$ equals $\boldsymbol{u} \cdot \boldsymbol{\nabla}p + p\boldsymbol{\nabla} \cdot \boldsymbol{u}$, and for a triply periodic domain, it has a vanishing volume average. Therefore, $-\langle \boldsymbol{u} \cdot \boldsymbol{\nabla}p \rangle = \langle p\boldsymbol{\nabla} \cdot \boldsymbol{u} \rangle$, highlighting that this term contributes to compressional heating. This term has been found to be significant in simulations of gravitational collapse (Brandenburg and Ntormousi 2021). We will see that when energy is injected through W_{L}, this energy is utilized to increase kinetic energy ($\dot{\mathcal{E}}_{\mathrm{K}} > 0$) and drive viscous heating.

The work done by the pressure force, W_{p}, is always small. Thus, we have the relationship:

$$W_{\mathrm{L}} = \dot{\mathcal{E}}_{\mathrm{K}} + \epsilon_{\mathrm{K}} - W_{\mathrm{P}}. \tag{31}$$

In our simulations, we adopted an isothermal equation of state, disregarding the evolution of thermal energy. If thermal energy were included, we would have:

$$\dot{\mathcal{E}}_{\mathrm{T}} = \epsilon_{\mathrm{M}} + \epsilon_{\mathrm{K}} - W_{\mathrm{P}}. \tag{32}$$

The thermal evolution, which accounts for the changes in thermal energy, plays a significant role in simulations related to thermal magneto-convection (Brandenburg, Jennings, et al. 1996). In such simulations, it aids in modeling buoyancy variations. Similarly, in simulations of the magneto-rotational instability, potential energy is converted into kinetic and magnetic energies, which subsequently dissipate as heat and radiation (Brandenburg, Nordlund, et al. 1995). However, for our specific objectives, it is adequate to focus on integrating the kinetic and magnetic

contributions over time. This involves calculating $\int \epsilon_K \, dt$ and $\int \epsilon_M \, dt$, respectively.

Now, let us discuss the interaction between electric and magnetic energies. This interplay is typically disregarded in the field of magnetohydrodynamics, where the evolution of the electric field, particularly the Faraday displacement current, is commonly omitted, according to Alfvén 1942. Taking the dot product of Equation (13) with $\boldsymbol{E}/\mu_0$ and using $1/(\mu_0 c^2) = \epsilon_0$, we obtain

$$\frac{\partial}{\partial t}\left(\epsilon_0 \boldsymbol{E}^2/2\right) = \frac{\boldsymbol{E}}{\mu_0 c^2} \cdot \frac{\partial \boldsymbol{E}}{\partial t} = \boldsymbol{E} \cdot \boldsymbol{\nabla} \times \boldsymbol{B}/\mu_0 - \boldsymbol{J} \cdot \boldsymbol{E}, \tag{33}$$

so, after averaging, we have

$$\frac{\mathrm{d}}{\mathrm{d}t}\left\langle \epsilon_0 \boldsymbol{E}^2/2 \right\rangle = \left\langle \boldsymbol{E} \cdot \boldsymbol{\nabla} \times \boldsymbol{B}/\mu_0 \right\rangle - \left\langle \boldsymbol{J} \cdot \boldsymbol{E} \right\rangle. \tag{34}$$

Next, we take the dot product of Equation (14) with $\boldsymbol{B}/\mu_0$ and obtain

$$\frac{\partial}{\partial t}\left(\boldsymbol{B}^2/2\mu_0\right) = -\boldsymbol{B} \cdot \boldsymbol{\nabla} \times \boldsymbol{E}/\mu_0. \tag{35}$$

In view of the $\left\langle \boldsymbol{E} \cdot \boldsymbol{\nabla} \times \boldsymbol{B}/\mu_0 \right\rangle$ term in Equation (34), it is convenient to rewrite Equation (35) in the form of

$$\frac{\partial}{\partial t}\left(\boldsymbol{B}^2/2\mu_0\right) = -\boldsymbol{E} \cdot \boldsymbol{\nabla} \times \boldsymbol{B}/\mu_0 - \boldsymbol{\nabla} \cdot (\boldsymbol{E} \times \boldsymbol{B}/\mu_0). \tag{36}$$

Again, given that the Poynting flux divergence vanishes under a triply periodic volume average, we have

$$\frac{\mathrm{d}}{\mathrm{d}t}\left\langle \boldsymbol{B}^2/2\mu_0 \right\rangle = -\left\langle \boldsymbol{E} \cdot \boldsymbol{\nabla} \times \boldsymbol{B} \right\rangle/\mu_0. \tag{37}$$

It is important to note the difference to Equation (17), which ignores the displacement current. An equation similar to Equation (17) can only be recovered for the sum of electric and magnetic energies, which yields

$$\frac{\mathrm{d}}{\mathrm{d}t}\left(\left\langle \boldsymbol{B}^2/2\mu_0 \right\rangle + \left\langle \epsilon_0 \boldsymbol{E}^2/2 \right\rangle\right) = -\left\langle \boldsymbol{J} \cdot \boldsymbol{E} \right\rangle. \tag{38}$$

An essential characteristic of well-conducting media in the context of magnetohydrodynamics is that the electric energy is typically considered to be significantly smaller or negligible when compared to the magnetic energy. In that limit, Equations (17) and (38) do indeed become equivalent.

More compactly, we can then write Equation (37) in the form $\dot{\mathcal{E}}_M = -Q_E$, where $Q_E = \left\langle \boldsymbol{E} \cdot \boldsymbol{\nabla} \times \boldsymbol{B} \right\rangle$ acts as a source in $\dot{\mathcal{E}}_E = Q_E - \epsilon_M - W_L$. Hence, it becomes evident that the electric energy reservoir is not merely a secondary component with limited energy content due to inefficient coupling. Instead, it serves as an indispensable intermediate stage through which magnetic energy is efficiently channeled onward, eventually contributing to kinetic and thermal energies. This realization prompts the question of how justifiable it is to neglect the displacement current, especially when, prior to the onset of conductivity, electric energy surpasses magnetic energy. This scenario is quite common in inflationary magnetohydrodynamic scenarios.

4.2 Electromagnetic and hydromagnetic waves

Brandenburg and Sharma 2021 discuss simulations of the early universe's evolution, focusing on electromagnetic fields, magnetic energy, and gravitational waves. The simulations are conducted within periodic cubic domains of different sizes, using various mesh points and spatial metrics, all scaled using conformal time. The speed of light is set to unity, and the Lorentz-Heaviside unit system is applied to the Maxwell equations. The simulations are divided into two steps. In the first step (Step I), they consider the end of reheating and solve the Maxwell equations with zero conductivity, accounting for the breaking of conformal invariance. In the second step (Step II), they transition into the radiation-dominated era, where the electric field becomes negligible, and the magnetic and gravitational wave fields are evolved. During these simulations, the importance of initializing the electric and magnetic fields were discussed to ensure a specific energy density ratio.

In a one-dimensional scenario and when the conductivity is zero, electromagnetic waves can indeed propagate in either the positive or negative x-direction. It's important to note that, in this case, the electric and magnetic energies are equal. However, as the conductivity becomes large, the magnitude of the electric field becomes suppressed. To comprehend this suppression, we need to examine Equation (13). As σ increases significantly, the need for balancing the $\boldsymbol{\nabla} \times \boldsymbol{B}$ term shifts from being regulated by the displacement current to being controlled by the actual current. By introducing $\boldsymbol{J} = \sigma \boldsymbol{E}$ (representing the comoving current density), we find $\boldsymbol{E} = \eta \boldsymbol{\nabla} \times \boldsymbol{B}$, implying that $|\boldsymbol{E}|/|c\boldsymbol{B}| = O(\eta k/c)$. Therefore, when σ reaches large values, $|\boldsymbol{E}|/c$ becomes notably reduced relative to $|\boldsymbol{B}|$. According to Brandenburg and Sharma 2021 for a linearly increasing conductivity profile, $(\sigma(t) = \sigma_{\max} t/t_{\mathrm{trans}})$ during a specific time interval $t_0 \leq t \leq t_0 + t_{\mathrm{trans}}$ with a duration of t_{trans} starting at $t = t_0$ here was a decrease in amplitude. The value of this amplitude drop increased approximately in inverse proportion to $\eta_{\min} k^2 t_{\mathrm{trans}}$, where $\eta_{\min} = 1/\mu_0 \sigma_{\max}$.

4.3 Conductivity as a function of time $\sigma(t)$

The linear σ profile used by Brandenburg and Sharma 2021 is given by

$$\sigma(t) = \sigma_{\min} + (\sigma_0 - \sigma_{\min}) \, \Theta(t), \tag{39}$$

where $\sigma_0 = 1/\mu_0 \eta_0$, $\sigma_{\min} = 1/\mu_0 \eta_{\max}$, and

$$\Theta = \max \left[\min \left(\frac{t - t_0}{\tau_0}, 1 \right), 0 \right] \tag{40}$$

is a piecewise linear function that goes from 0 (for $t \leq t_0$) to 1 (for $t \geq t_0 + \tau_0$).

We also study a profile whose logarithm is linearly varying. We, therefore, refer to it as a logarithmic profile, which is of the form

$$\sigma(t) = \sigma_0 \exp \left\{ \ln(\sigma_{\max}/\sigma_0) \left[1 - \Theta(t) \right] \right\}. \tag{41}$$

This implies

$$\ln \eta(t) = \ln \eta_0 + (\ln \eta_{\max} - \ln \eta_0) \left[1 - \Theta(t) \right]. \tag{42}$$

This approach enables us to determine the duration over which σ transitions by a factor of ten (an order of magnitude) for any given value of σ. In contrast, with a linear σ profile, the duration would vary across different ranges of σ values, and it would be exceptionally brief for large values of σ.

4.4 Simulating the transition of Alfvén waves

Here, $\boldsymbol{\nabla} \times \boldsymbol{A}$ represents the departure from the initially imposed magnetic field. Together with the constant magnetic field B_{x0} in the x-direction, we have $\boldsymbol{B} = (B_{x0}, -\partial A_z/\partial x, 0)$. In the subsequent numerical experiments, we adopt $t = -10$ to initiate the simulations. In Figure 2 we compare the behavior of $B_y(x, t)$ as depicted in a colored contour plot in the xt plane. These simulations were conducted within a domain of size $L = 2\pi$, where the lowest wave number is $k_1 = 2\pi/L = 1$. Initially, the density is uniform and equal to ρ_0.
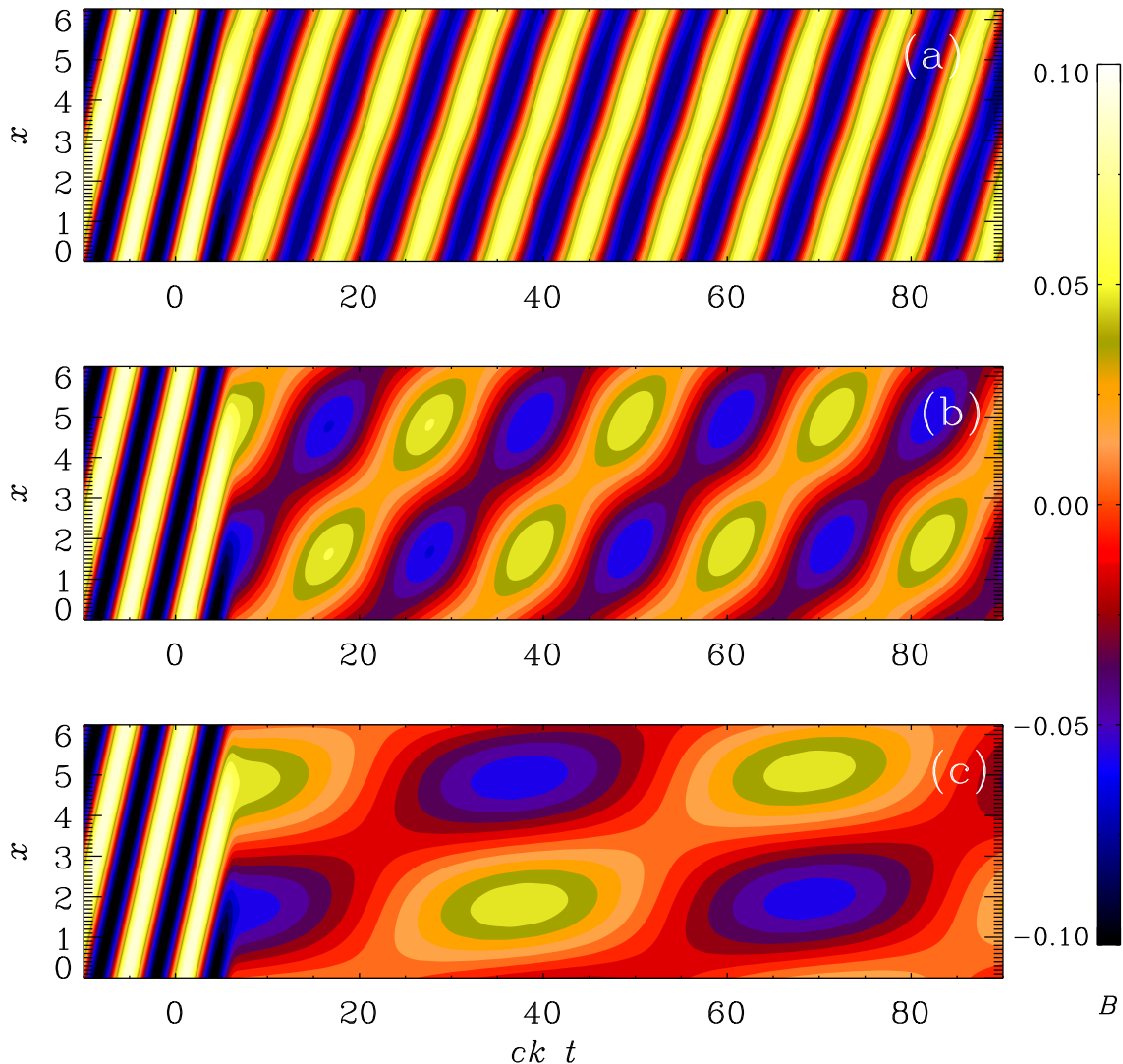
Figure 2: Evolution of $B_y(x, t)$ for the logarithmic σ profile with (**a**) $v_{A0} = 1$, (**b**) $v_{A0} = 0.3$, and (**c**) $v_{A0} = 0.1$, and $t_{\mathrm{trans}} = 10$ in all cases. Note the transition to conductivity at $t = t_0 \equiv 0$.

We see that for $v_{A0} = 0.3$ and 0.1, the transition to Alfvén waves is accompanied by a wobble in the magnetic field. To understand this and test the dependence on the initial velocity for Alfvén waves, we show in Figure 3 the results for standard MHD simulations (without displacement current) with different initial amplitudes, `ampl_uz=.1` (the usual case), `ampl_uz=.05` (reduced initial velocity), and `ampl_uz=0` (no velocity). We see that the wobble seen in Figure 2(b) is well reproduced by an intermediate value of the initial velocity. For the simulation with $v_{A0} = 1$, on the other hand, the conversion to Alfvén waves is more efficient and the required level of the velocity is readily achieved.
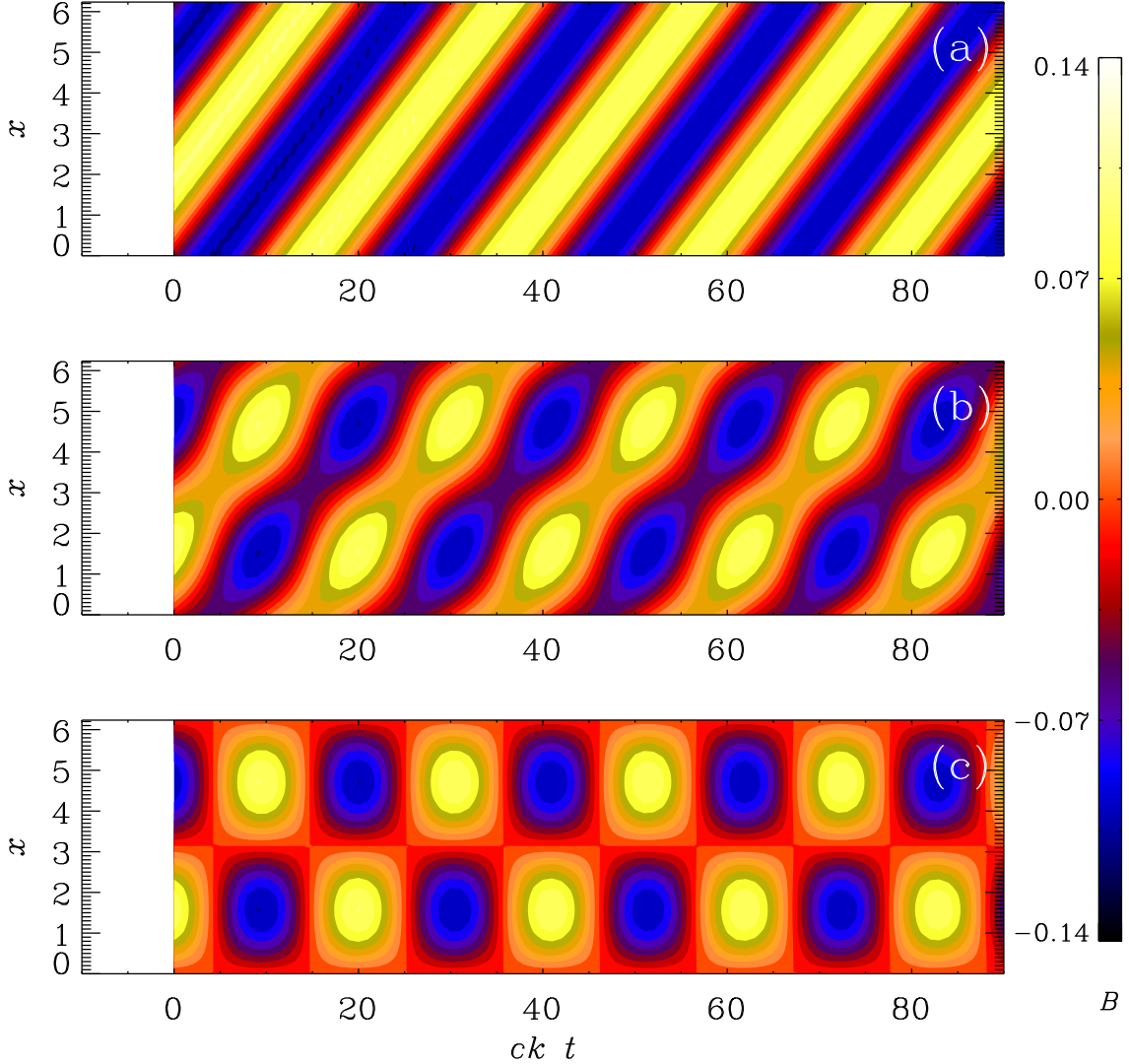
Figure 3: Evolution of $B_y(x,t)$ for Alfvén waves with constant σ with (**a**) `ampl_uz=.1`, (**b**) `ampl_uz=.05` and (**c**) `ampl_uz=0`. Here, the initial condition has been imposed at $t = 0$.

In Figure 4 we compare the evolution of $B_y(x,t)$ for the logarithmic σ profile with the linear one, setting $v_A = 0.3$. It's evident that the logarithmic profile exhibits a significantly more pronounced drop in amplitude compared to the linear σ profile. As we will see below, this is because for a logarithmic profile, the system spends considerably more time with $R(t) \approx 1$ than for the linear profile. Achieving a comparable decrease with the linear σ profile would necessitate an extension of t_{trans} to approximately 500, as illustrated in Figure 4(**c**).

25
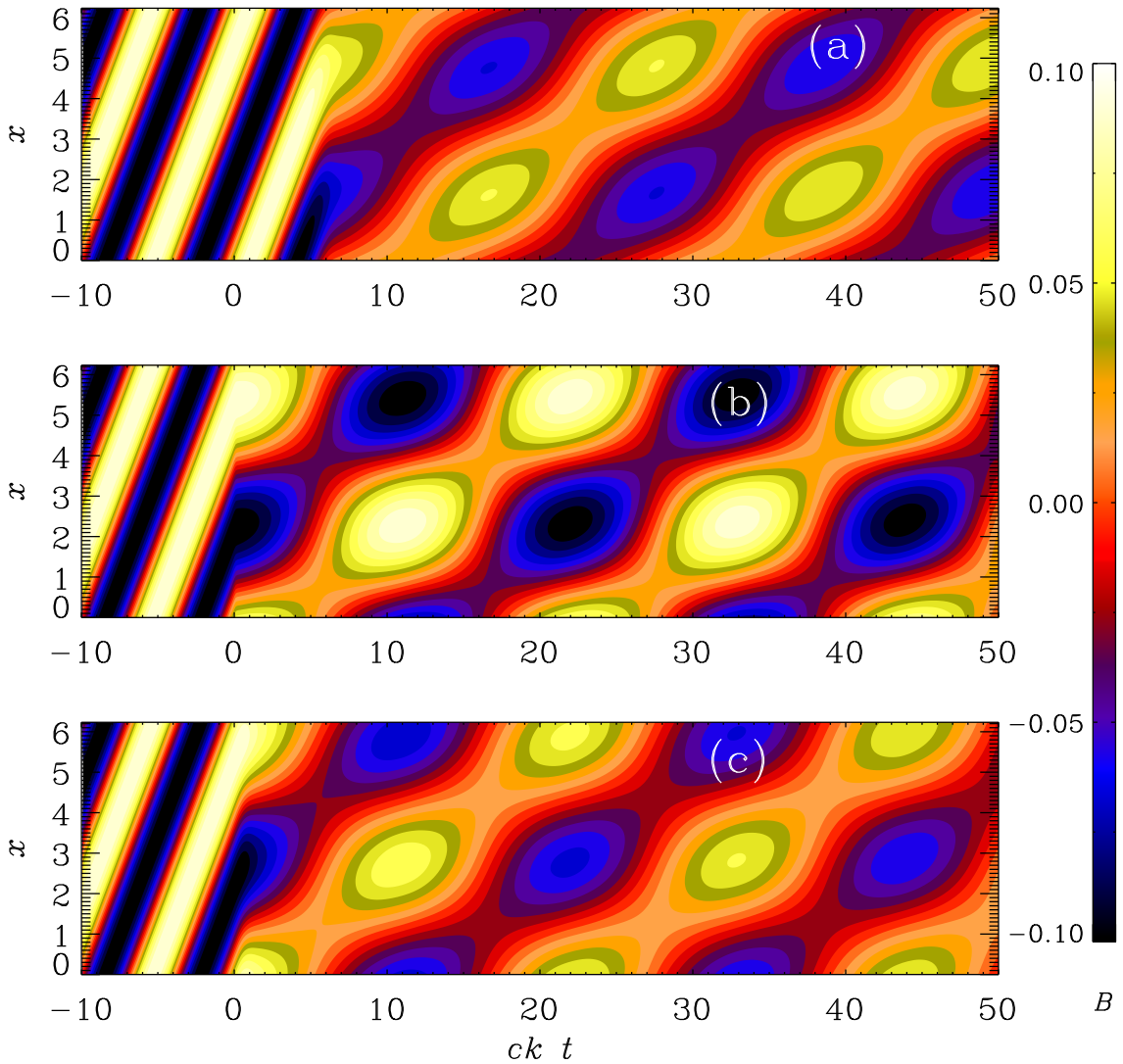
Figure 4: Evolution of $B_y(x,t)$ for the logarithmic σ profile with $v_\text{A} = 0.3$ and (**a**) the logarithmic σ profile with $t_\text{trans} = 10$, (**b**) the linear σ profile with $t_\text{trans} = 10$, and (**c**) the linear σ profile with $t_\text{trans} = 500$.

For a more quantitative analysis, we need to examine Figure 5(**a**) where we compare the temporal evolution of B_y at a specific location, denoted as $x = x_*$, for the three simulations presented in Figure 4(**a**) and (**c**). It is worth noting that the reduction in wave amplitude following $t = 0$ appears similar for runs (**a**) and (**c**) while it is significantly less pronounced for run (**b**). In Figure 5(**b**) we provide a depiction of how the parameter σ varies over time. To quantify the decay behavior, we employ a nondimensional resistivity, denoted as $R(t)$, defined as $R(t) \equiv \eta(t)k/c$. This quantity exhibits a substantial decrease from 10^4 to 5×10^{-4}. Notably, a majority of this decay transpires during the period when $R(t)$ undergoes a transition near unity. Due to the logarithmic nature of the profile, $R(t)$ spends approximately $ckt_\text{trans} = 5$ units of time while transitioning from 10 to 0.1 in value. Conversely, for the linear profile, this time interval is nearly nonexistent. However, when we extend t_trans to 500 we observe that ckt_trans becomes similar to the values that led to a comparable decay in the logarithmic profile. This observation is corroborated by the inset shown in panel (**b**) illustrating that $R(t)$ crosses the unity threshold by approximately an order of magnitude for cases (**a**) and (**c**), but

26

not for case (**b**). These findings substantiate the significance of the time interval where $R(t)$ is approximately within an order of magnitude of unity.
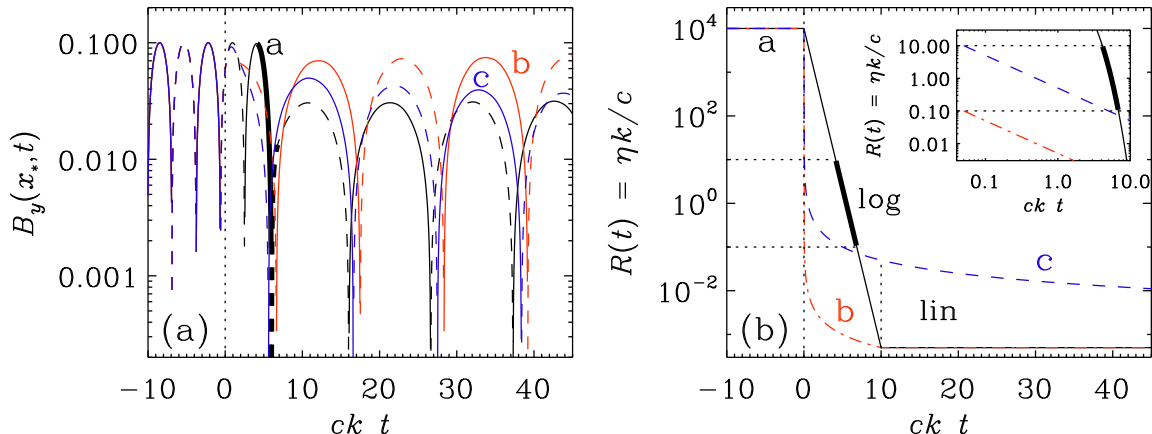
Figure 5: (**a**) Evolution of B_y at one specific point $x = x_*$ in the three runs of Figure 4a,c. Note that the drop of the wave amplitude after $t = 0$, and specifically at $t = 50$, is similar for runs a and c, but much less for **b**. (**b**) Dependence of the nondimensional resistivity $R(t) = \eta(t)k/c$ for the logarithmic profile with $t_{\text{trans}} = 10$ in run a (black), and the linear profile with $t_{\text{trans}} = 10$ in run b (red) and $t_{\text{trans}} = 500$ in run c (blue). The inset shows a blow-up of a narrow strip around $R = 1$ using a logarithmic time axis. We see from the inset that the time spent in $R(t)$ traversing unity by a margin of one order of magnitude (marked by the thick part of the black line) is similar for runs a and c, but virtually non-existing for run b.

The evolution of electric, magnetic and kinetic energy densities, as well as the two contributions to thermal energy, $\int \epsilon_M \, dt$ and $\int \epsilon_K \, dt$, are shown in Figure 6. Examining Figure 6, it becomes apparent that the electric energy initially matched the magnetic energy. However, as the conductivity increases, there is a swift reduction in electric energy ($\dot{\mathcal{E}}_E < 0$), with the majority of it dissipating as thermal energy, $\int \epsilon_M \, dt$. Only a small portion, amounting to less than 20% for $t_{\text{trans}} = 10$, is channeled into kinetic energy. Remarkably, the average energy densities for both magnetic and electric fields exhibit a decay pattern governed by $\exp(-\nu k^2 t)$. Notably, this decay does not feature a factor of 2 in the exponent.

This behavior signifies not a transformation of kinetic energy, which would be proportional to $\exp(-2\nu k^2 t)$, but rather a change in velocity, a contribution introduced through the work term W_L, which is linear in the velocity. Furthermore, it is noteworthy that the ratio $\mathcal{E}_E/\mathcal{E}_M$ remains at approximately 10 for $\text{Pr}_M = 20$. Additionally, it is worth mentioning that the oscillations in the sum of magnetic and kinetic energies ($\mathcal{E}_M + \mathcal{E}_K$, represented by the orange lines) are predominantly balanced by oscillations in electric energy ($\mathcal{E}_E$, depicted by the blue lines).
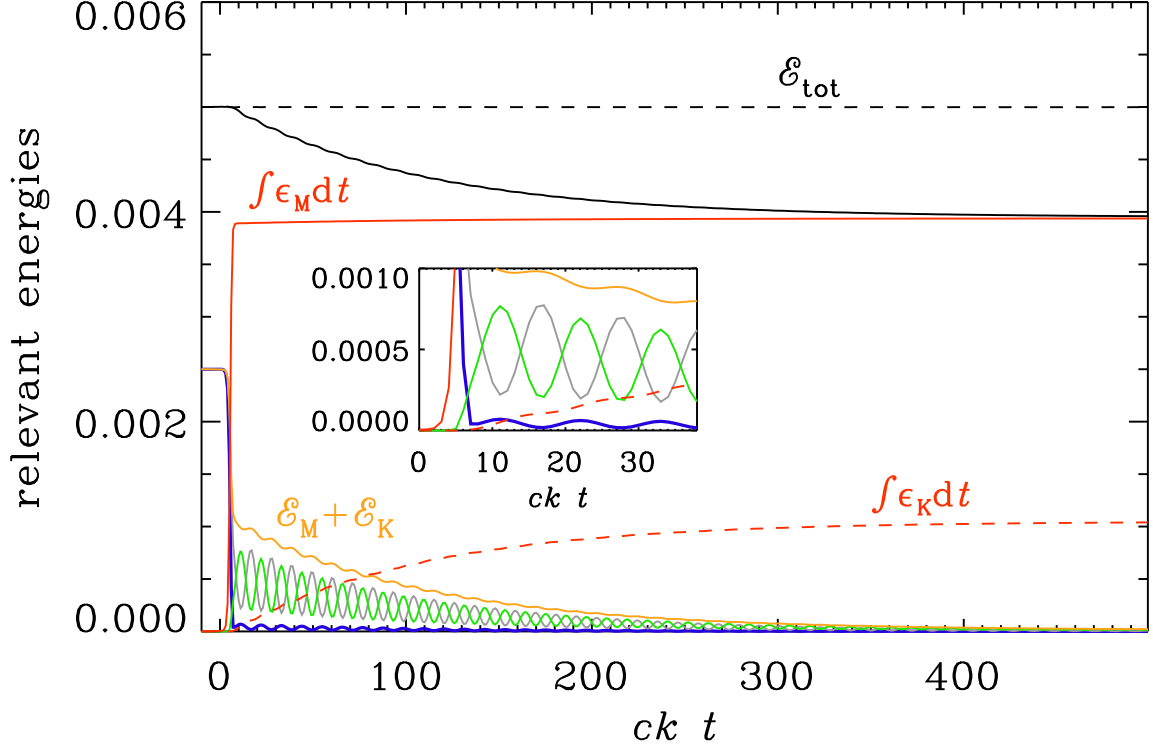
Figure 6: Initially, all the energy is in electromagnetic energy, $\mathcal{E}_E + \mathcal{E}_M$ for $\nu = 0.01$ and $\eta_{\text{fin}} = 5 \times 10^{-4}$. In the end, all the energy is converted into heat. The red lines give the integrated Ohmic and viscous energy gains, $\int \epsilon_M \, dt$ and $\int \epsilon_K \, dt$, respectively. At intermediate times, this energy is distributed to equal amounts among kinetic energy $\mathcal{E}_K$ (green lines) and magnetic energy $\mathcal{E}_M$ (gray lines). The orange lines shows their sum, $\mathcal{E}_K + \mathcal{E}_M$. The blue lines represent $\mathcal{E}_E$. The inset shows a blow-up of the same graph around the origin. We see that $\mathcal{E}_E$ varies in phase with $\mathcal{E}_K$, but an anti-phase both with $\mathcal{E}_M$ and the residual $\mathcal{E}_M + \mathcal{E}_K$.

From Figure 6, we have seen that W_L/ϵ_M is always small, but it becomes even smaller when t_{trans} is large. Therefore, the drop of magnetic energy after the transition should increase with t_{trans}.

In Figure 7 we present the temporal evolution of various energy fluxes. It becomes evident that magnetic energy progressively diminishes and releases energy into the electric energy reservoir, facilitated by the term $Q_E = \langle \boldsymbol{E} \cdot \boldsymbol{\nabla} \times \boldsymbol{B} \rangle > 0$. Therefore, magnetic heating encompasses the following components:

$$\epsilon_M = -\dot{\mathcal{E}}_E + Q_E - W_L. \tag{43}$$

For swift transitions with $t_{\text{trans}} \lesssim 5$, Q_E is relatively small in comparison to $-\dot{\mathcal{E}}_E$. Consequently, ϵ_M primarily results from the depletion of electric energy ($\dot{\mathcal{E}}_E < 0$). However, for extended transitions ($t_{\text{trans}} > 10$), Q_E approximately equals $-\dot{\mathcal{E}}_E$. In this case, ϵ_M is contributed to approximately 50% by Q_E and the remaining 50% by $-\dot{\mathcal{E}}_E$.
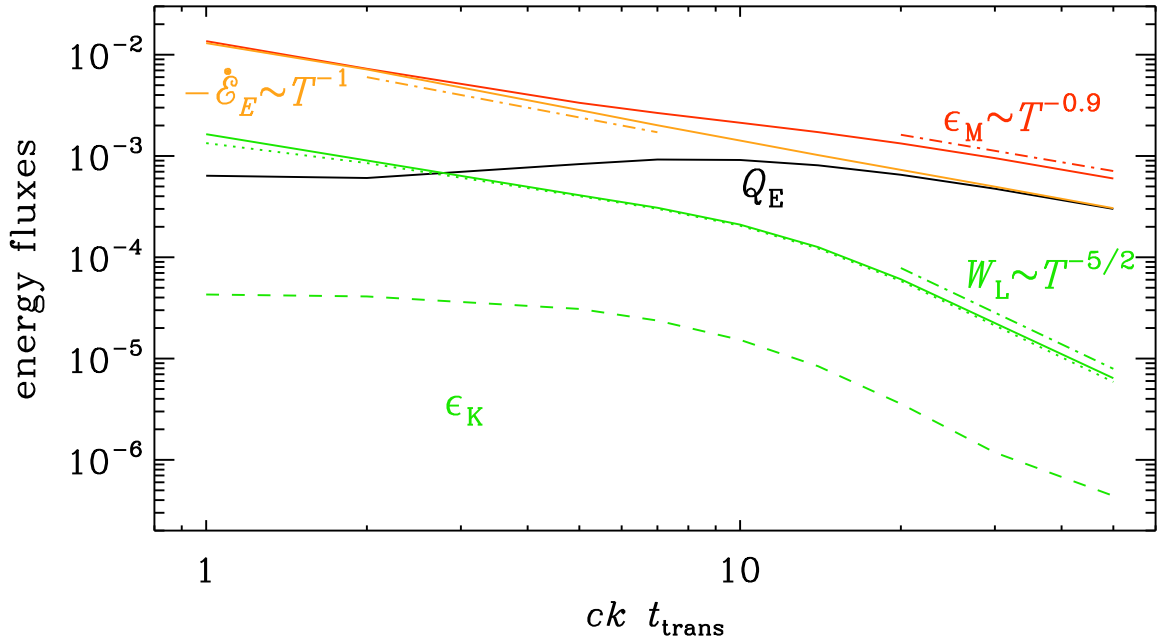
Figure 7: Evolution of energy fluxes for the model with the logarithmic conductivity profile with $\eta = 5 \times 10^{-4} = \nu$ at late times. In all cases, the initial diffusivity is $\eta_{\mathrm{ini}} = 10^4$. The main difference to the run with a larger viscosity is that ϵ_{K} is larger.

In Figure 8 we provide a quantitative representation of the energy drop (loss of magnetic energy) phenomenon by plotting the magnetic energy ($\mathcal{E}_{\mathrm{M}}$) at $t = 100$ which corresponds to a point in time when the conductivity has substantially increased. This is done for various values of t_{trans} and v_{A0}/c. Notably, we observe that the slope of this curve diminishes as the Alfvén wave speed increases.
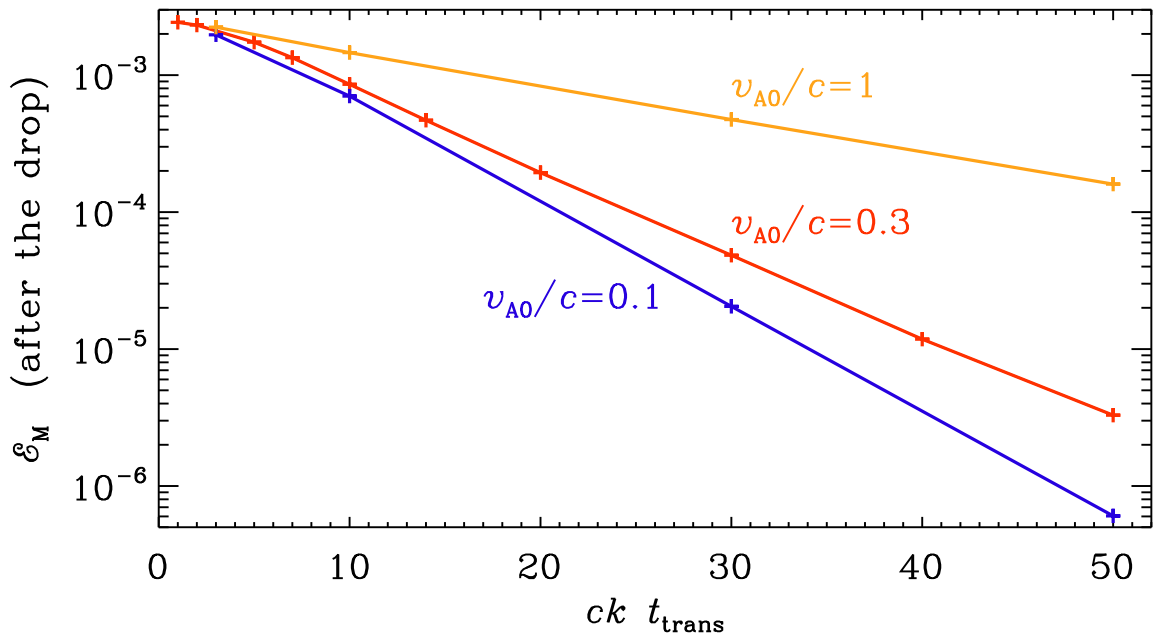
Figure 8: $\mathcal{E}_{\mathrm{M}}$ at $t = 100$, i.e., after the conductivity has increased to large value, vs. t_{trans} for $v_{\mathrm{A0}}/c = 1$ (orange), $v_{\mathrm{A0}}/c = 0.3$ (red), and $v_{\mathrm{A0}}/c = 0.1$ (blue).

29

4.5 Application to cosmological magnetic fields

As discussed in Brandenburg and Sharma 2021, magnetic fields are constantly being generated through dynamo action on various scales in the present universe. This regeneration is driven by gravitational energy released during processes like accretion or direct collapse.

In the vast regions between galaxy clusters known as "voids," it is generally believed that contemporary dynamo action cannot produce magnetic fields.

In addition, there is indirect evidence suggesting the presence of magnetic fields in voids, which are difficult to explain via dynamo action. This evidence comes from observations related to blazars. The presence of magnetic fields on very large cosmological scales could be of primordial origin. These fields might have been created during or before the radiation-dominated era of the universe, possibly during cosmological phase transitions or inflation. The role of electromagnetic fields in transitioning to magnetohydrodynamic fields during inflation is of particular interest.

4.6 Avoiding the discontinuity in the generation term

In Brandenburg and Sharma 2021, the switch from a vacuum to a conducting Universe was modelled as a discontinuous switch, where f''/f jumped from $1/2$ to zero. To avoid this, we need a version of $a(t)$ where all its derivatives are continuous. Following the work of He, Roper Pol, and Brandenburg 2023, we do this by solving the Friedmann equation.

There are two actually independent Friedmann equations. The first one is

$$\frac{\dot{a}^2 + Kc^2}{a^2} = \frac{8\pi G\rho}{3}, \tag{44}$$

and the second one is given by

$$\frac{\ddot{a}}{a} = -\frac{4\pi G}{3}\left(\rho + \frac{3p}{c^2}\right) + \frac{\Lambda c^2}{3}. \tag{45}$$

Here, a is the scale factor.

Using the Hubble parameter, $H \equiv \dot{a}/a$ and the first equation, the second one can be rewritten as,

$$\dot{\rho} = -3H\left(\rho + \frac{p}{c^2}\right). \tag{46}$$

These equations can be simplified as

$$H^2 = \left(\frac{\dot{a}}{a}\right)^2 = \frac{8\pi G}{3}\rho - \frac{Kc^2}{a^2}. \tag{47}$$

$$\dot{H} + H^2 = \frac{\ddot{a}}{a} = -\frac{4\pi G}{3}\left(\rho + \frac{3p}{c^2}\right). \tag{48}$$

Then, a density parameter (Ω) is introduced which is the ratio of the actual (or observed)

density ρ to the critical density ρ_c of the Friedmann universe.

$$\Omega \equiv \frac{\rho}{\rho_c} = \frac{8\pi G\rho}{3H^2}. \tag{49}$$

The Friedmann equations, which describe the evolution of the universe in the framework of general relativity, can be solved exactly in the presence of a perfect fluid with a specific equation of state,

$$p = w\rho c^2 \tag{50}$$

where p is the pressure, ρ is the mass density of the fluid in the comoving frame and w is some constant that characterizes the type of fluid. The exact solutions to the Friedmann equations depend on the value of w

and the curvature of the universe K. When w is approximately zero (for non-relativistic matter like dark matter or non-relativistic particles), the exact solution leads to the matter-dominated era, where the scale factor of the universe grows with time as a power of t ($a \propto t^{2/3}$). For radiation, such as photons, w is equal to $1/3$. The exact solution leads to the radiation-dominated era, where the scale factor grows faster than in the matter-dominated era ($a \propto t^{1/2}$) in a radiation-dominated universe). When w is equal to -1 (for dark energy with a cosmological constant Λ), the exact solution corresponds to a universe dominated by dark energy. The curvature of the universe, described by the parameter K (which can be 0, 1, or -1 for flat, closed, or open universes, respectively), also plays a role in determining the exact solutions to the Friedmann equations.

In the following, we work with conformal time η; see Section 2.2. In that case, the growth of the scale factor with conformal time is $a \propto \eta$ during the radiative era when $w = 1/3$, $a \propto \eta^2$ during the matter-dominated era and during reheating when $w = 0$, and $a \propto (1 - H\eta)^{-1}$ during inflation when $w = -1$. However, to avoid confusion with the magnetic diffusivity, which was also called η, to still denote the conformal time by t.

4.7   Results for magnetogenesis around the end of reheating

In Figure 9 we illustrate the evolution of electric energy ($\mathcal{E}_{\mathrm{E}}$), magnetic energy ($\mathcal{E}_{\mathrm{M}}$) and kinetic energy ($\mathcal{E}_{\mathrm{K}}$) for $k = 10$ across three distinct values of β: 1, 2, and 4. Throughout these simulations, the initial amplitudes were adjusted so that $\mathcal{E}_{\mathrm{M}} = 10^{-4}$ at $t = t_0$. In all cases, the solutions have stabilized by $t = t_0 = 1$. Notably, we observe electromagnetic oscillations as we approach the conclusion of the reheating phase, occurring just before the onset of conductivity at $t_0 = 1$.

When simulating the transition from a vacuum to high conductivity and the accompanying Joule heating, it's essential to make specific choices regarding when the conductivity, σ, should begin to increase. This involves selecting values for t_0 (the starting time) and t_{trans} (the transition duration). If t_0 is chosen to be excessively large, the solutions will depict the establishment of electromagnetic waves well before the transition, as illustrated in Figure 9. In this figure, we note that the smallest wavenumber in the one-dimensional domain is $k = 10$. Therefore, by

the time $t = 1$, even the largest modes within the domain have become stable. Additionally, at early times, the electric energy ($\mathcal{E}_E$) and magnetic energy ($\mathcal{E}_M$) grow in an algebraic manner and then transition into oscillatory behavior when $k_*(t)$ falls below k. When conductivity is switched on at $t = t_0 = 1$, the electric energy diminishes rapidly, while the magnetic energy declines at a much slower pace. However, the generated hydrodynamic energy remains relatively low.
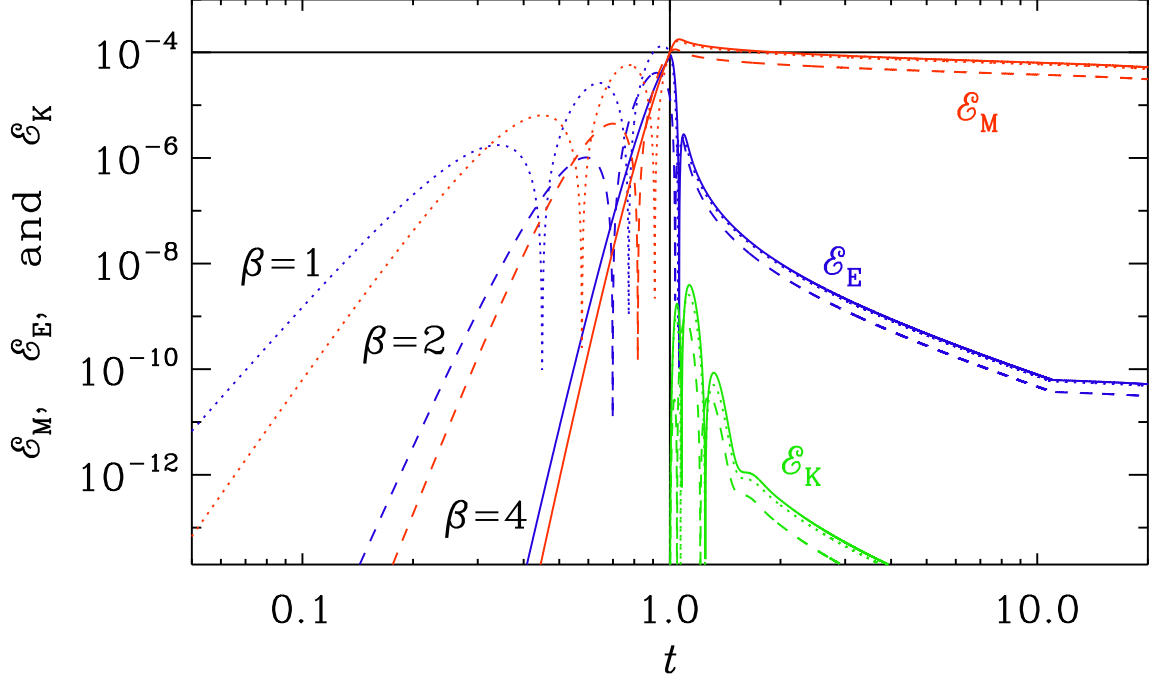
Figure 9: t dependence of $\mathcal{E}_M$ (red), $\mathcal{E}_E$ (blue), and $\mathcal{E}_K$ (green) for runs with $\beta = 1$ (dotted lines), 2 (dashed lines), and 4 (solid lines) for Set (i) with $k = 10$, $t_0 = 1$, and $t_{\mathrm{trans}} = 10$. The initial amplitudes have been arranged such that $B_{\mathrm{rms}} = 0.01$ at $t = 1$. From the double-logarithmic representation, we see that the growth of $\mathcal{E}_M$ and $\mathcal{E}_E$ is algebraic, and much faster for the models with a larger value of β. Before $t = 1$, $\mathcal{E}_E$ dominates over $\mathcal{E}_M$, but drops immediately after $t = 1$, when resistivity emerges and kinetic energy is being generated. Both $\mathcal{E}_M$ and $\mathcal{E}_K$ are larger for larger values of β.

In the following sets of simulations, our aim is to explore scenarios different from Figure 9. In Set (ii), we choose parameters $k = 10$, $t_0 = 0.1$, and $t_{\mathrm{trans}} = 1$ (as shown in Figure 10), while in Set (iii), we use $k = 1$, $t_0 = 1$, and $t_{\mathrm{trans}} = 10$ (as presented in Figure 11). In both cases, the electric energy decreases significantly when conductivity is activated. However, there is a notable difference in the maximum magnetic energies achieved for the three cases with $\beta = 1$, 2, and 4. Specifically, for $\beta = 4$ the kinetic energy ($\mathcal{E}_K$) reaches approximately one percent of the magnetic energy ($\mathcal{E}_M$) at $t = 0.2$.
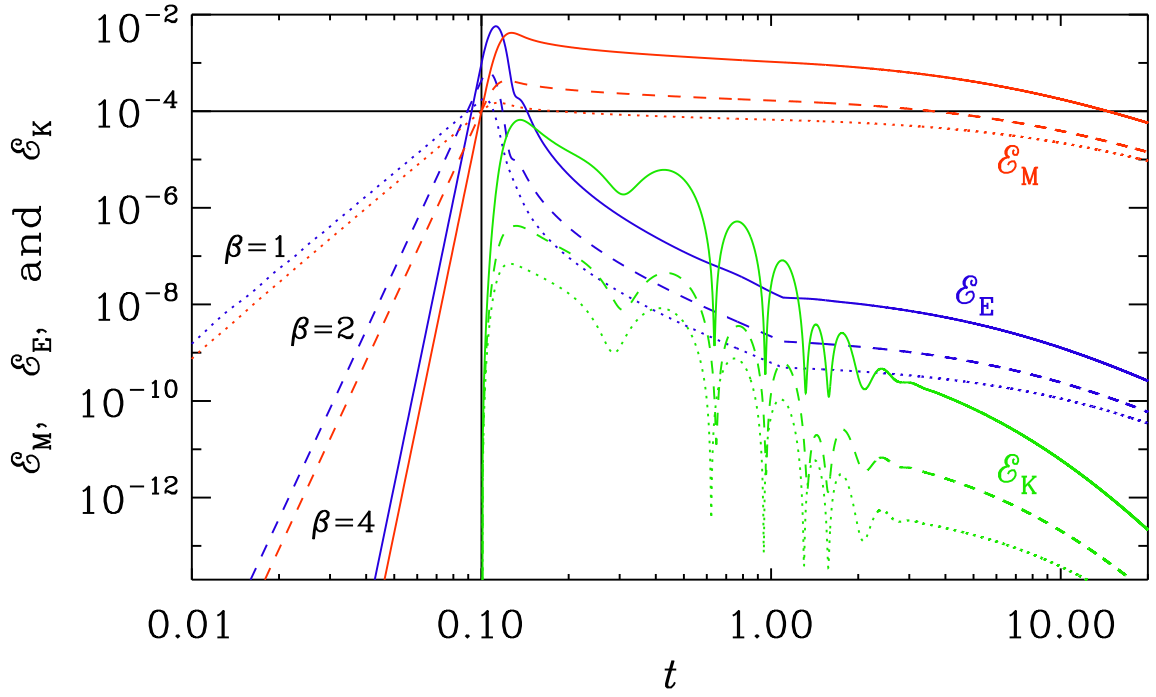
Figure 10: Similarly to Figure 9, but for Set (ii) with $k = 10$, $t_0 = 0.1$, and $t_{\text{trans}} = 1$.
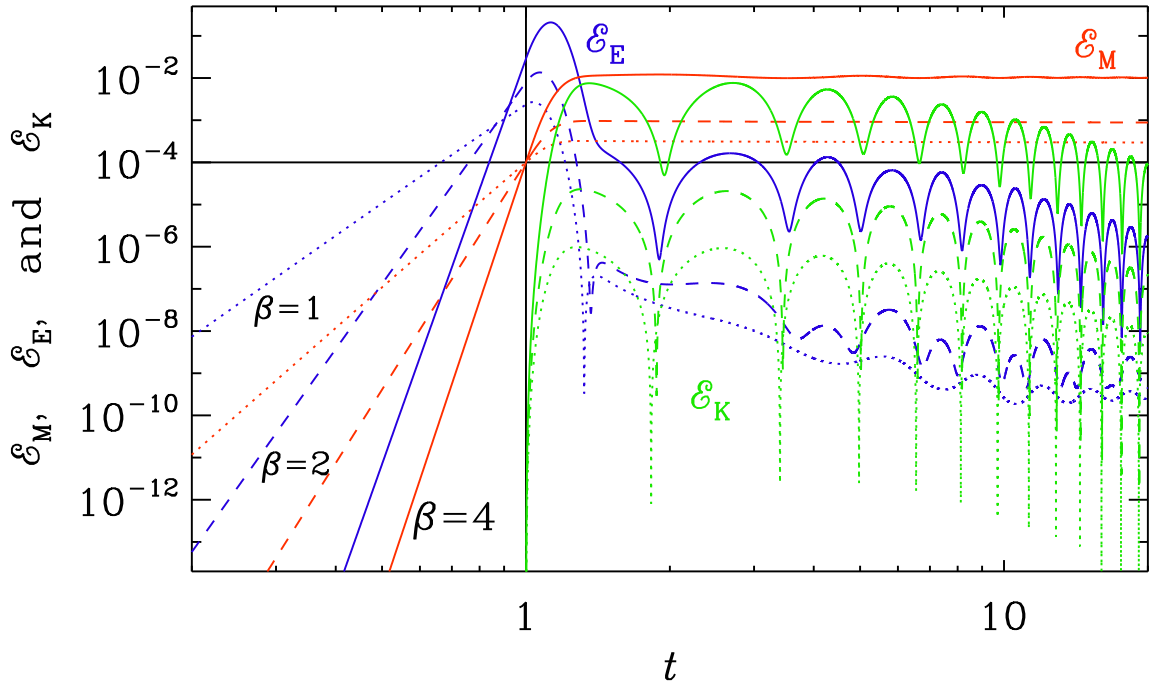
Figure 11: Similarly to Figure 9, but for Set (iii) with $k = 1$, $t_0 = 1$, and $t_{\text{trans}} = 10$.

4.8 Source of electric energy during reheating

We recall that in Equation (1) we considered the scaled magnetic vector potential $\boldsymbol{\mathcal{A}} \equiv f\boldsymbol{A}$. To describe the flow of energy properly, it is convenient to return to the formula for $\boldsymbol{A}$, which

reads (Subramanian 2010)

$$\left[\frac{1}{c^2} \left(\frac{\partial^2}{\partial t^2} + \frac{2f'}{f} \frac{\partial}{\partial t} \right) - \nabla^2 \right] \boldsymbol{A} = 0. \tag{51}$$

Compared with the original Ampere's law (12), the conformal invariance breaking leads to a modification of the displacement current, so the Ampere's law therefore reads

$$\frac{1}{c^2} \left(\frac{\partial \boldsymbol{E}}{\partial t} + \frac{2f'}{f} \boldsymbol{E} \right) = \boldsymbol{\nabla} \times \boldsymbol{B} - \mu_0 \boldsymbol{J}. \tag{52}$$

Taking the dot product with $\boldsymbol{E}$, we then obtain after volume averaging the evolution equation for the electric energy in the form

$$\frac{\mathrm{d}}{\mathrm{d}t} \left\langle \epsilon_0 \boldsymbol{E}^2/2 \right\rangle = -2(f'/f) \left\langle \epsilon_0 \boldsymbol{E}^2 \right\rangle + \left\langle \boldsymbol{E} \cdot \boldsymbol{\nabla} \times \boldsymbol{B}/\mu_0 \right\rangle - \left\langle \boldsymbol{J} \cdot \boldsymbol{E} \right\rangle. \tag{53}$$

Now, comparing Equation 53 with 34, we can see that we have an extra term, $Q_{\mathrm{G}} = -2(f'/f) \left\langle \epsilon_0 \boldsymbol{E}^2 \right\rangle$, which corresponds to the energy input Q_{G} if $f'/f < 0$.

This is indeed the case during reheating, when $f \propto a^{-\beta} \propto t^{-2\beta}$ is assumed, because in that case, we have

$$\frac{f'}{f} = -\frac{2\beta}{t}, \tag{54}$$

which makes $Q_{\mathrm{G}} = -2(f'/f) \left\langle \epsilon_0 \boldsymbol{E}^2 \right\rangle$ in the RHS of Equation 53 positive for $\beta > 0$. By comparison, in the model of Sharma, Jagannathan, et al. 2017, we expect to have $f \propto a^\alpha$ with $\alpha > 0$ during inflation. Thus, with $a \propto (1 - Ht)^{-1}$ and $a'/a = H/(1 - Ht)$, we have $f'/f = \alpha H$, so now $Q_{\mathrm{G}} < 0$, and energy is therefore drawn out of the system, so the electric energy decreases. Thus, during that time, only the function $\boldsymbol{\mathcal{A}} \equiv f \boldsymbol{A}$ of Subramanian 2010 increases, but not $\boldsymbol{A}$ itself.
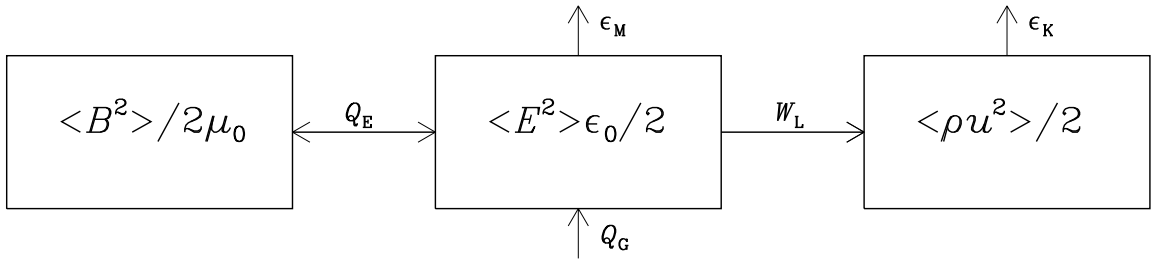
Figure 12: Similar to Figure 1, but now with inflationary magnetogenesis energy generation and energy exchange between electric and magnetic energies in both directions.

In Figure 12 we see that the current situation involves a system that is energetically driven by the input of energy through the Q_{G} term. It is enlightening to express the electric energy equation as follows:

$$Q_{\mathrm{G}} = \epsilon_{\mathrm{M}} + \dot{\mathcal{E}}_{\mathrm{E}} + W_{\mathrm{L}} - Q_{\mathrm{E}}. \tag{55}$$
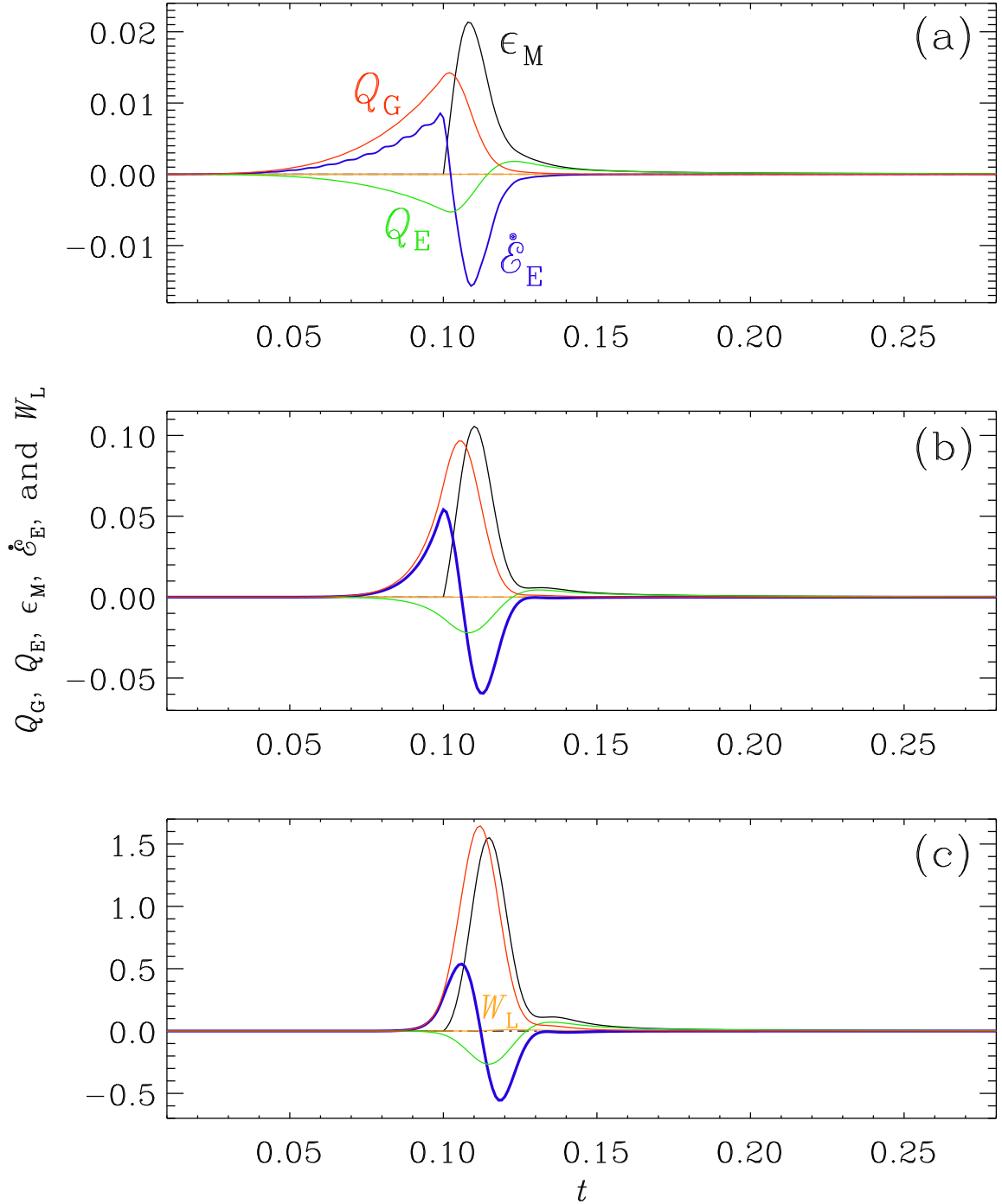
Figure 13: Time dependence of Q_G (red), Q_E (green), ϵ_M (black), $\dot{\mathcal{E}}_E$ (blue), and W_L (orange) for the runs of Set (ii) in Figure 10 with (**a**) $\beta = 1$, (**b**) $\beta = 2$, and (**c**) $\beta = 4$ for $t_0 = 0.1$ and $t_{\text{trans}} = 1$.

When comparing the three panels in Figure 13, it becomes evident that for $\beta = 1$, there is a gradual generation phase (see the red line for Q_G) that initiates well before t_0.

Let us call this Phase I. During that time, $\dot{\mathcal{E}}_E > 0$, but $Q_E < 0$, so part of the electric energy is converted into magnetic energy. In the second phase, which we call Phase II, we have $\dot{\mathcal{E}}_E < 0$. This phase starts when $t = t_0$ and it also coincides with the maximum of Q_G and the negative extremum of Q_E. Somewhat later, however, Q_E changes sign and becomes positive, so now magnetic energy is converted back into electric energy. Nevertheless, $\dot{\mathcal{E}}_E$ remains negative,

35

so electric energy still decreases. This is because all this energy is immediately converted onto heat and mechanical energy through a negative W_L, although this term is rather small by comparison. It is important to note, however, that the vertical axis scales differ across the panels.

To see whether more mechanical energy is being producing in the models of series (iii), we show a corresponding plot of energy fluxes in Figure 14. Since this plot is on a linear scale, unlike that of Figure 11, the resulting W_L term appears still rather small. Upon closer inspection, however, we can see that the ratio of the maxima of W_L and ϵ_M has increased from 0.007 to 0.01.
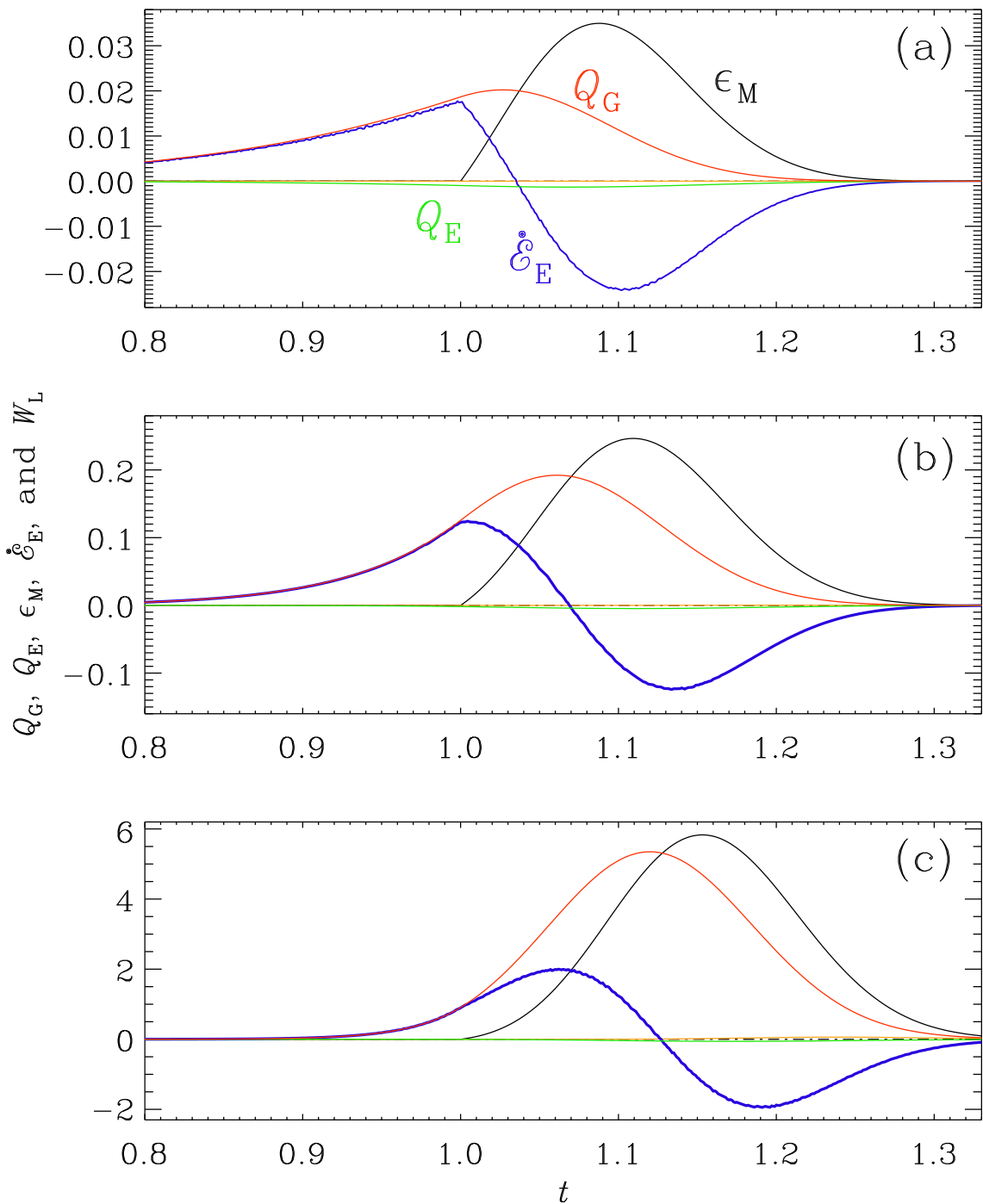
Figure 14: Similarly to Figure 13, but now for Set (iii) with $k = 1$, $t_0 = 1$, and $t_{\text{trans}} = 10$.

5 Discussion

This study has demonstrated that the Lorentz force can perform significant work when the conversion of electromagnetic energy takes place early and on sufficiently large scales to ensure that the modes are still growing in time. This phenomenon arises due to a substantial surplus of electric energy over magnetic energy. When conductivity emerges, this electric energy is not just lost, but a sizeable fraction is converted into magnetohydrodynamic energy. Notably, this effect has been overlooked in previous simulations related to inflationary magnetogenesis, especially in investigations of the additional contributions to the resulting production of relic gravitational waves.

For the survival of a significant amount of magnetic energy in the radiation-dominated era, it is beneficial, if the emergence of conductivity happens rapidly, i.e., if $ckt_{\rm trans} \leq 10$; see Figure 7. For larger values of $ckt_{\rm trans}$, most of that energy is converted into heat and only a small fraction survives as hydromagnetic energy, as noted above. It also matters when the transition to conductivity occurs, because the excess of electric energy over magnetic energy decreases toward the end of the reheating phase. In particular, we found that $tE_{\rm rms}/B_{\rm rms} \approx \beta + 1$, see Brandenburg and Protiti 2023 for details. It would therefore be useful to find out more about the particular way of how electric conductivity emerges.

In hindsight, it would have been useful to consider also larger values of β. The largest value of β considered in the work of Brandenburg and Sharma 2021 was $\beta = 10$. In general, however, the value of β should be calculated selfconsistently, depending on the assumed energy scale of reheating. All the models of Brandenburg and Sharma 2021 assumed a relatively low reheating energy scale between $3 \times 10^5 \, {\rm GeV}$, where $\beta = 1.7$ was obtained, and $0.15 \, {\rm GeV}$, the QCD energy scale, where $\beta = 3$ was used for a particular choice of the original electric and magnetic energy spectra at the end of inflation. Larger values of $\beta = 7.7$ were derived for a particular model with a reheating temperature of $10 \, {\rm GeV}$ and an initial k^{-3} spectrum for the magnetic energy.

It would also be useful to reconsider the differences between helical and nonhelical magnetogenesis. The simulations of Brandenburg, He, and Sharma 2021 have focused on the resulting gravitational wave production and found that their efficiency is similar for helical and nonhelical inflationary magnetogenesis simulations.

Extending our research to turbulent flows and magnetic fields would be a valuable next step. Achieving this involves solving for the evolution of the electric charge density, $\rho_{\rm e}$, while ensuring that $\boldsymbol{\nabla} \cdot \boldsymbol{E} = \rho_{\rm e}/\epsilon_0$ is consistently satisfied. In the presence of the magnetogenesis mechanism, the evolution equation for $\rho_{\rm e}$ can be given by

$$\frac{\partial \rho_{\rm e}}{\partial t} + \frac{2f'}{f} \rho_{\rm e} = -\boldsymbol{\nabla} \cdot \boldsymbol{J}. \tag{56}$$

It is worth noting that this constraint was automatically adhered to in our one-dimensional models. In the future, exploring dynamo action in scenarios with moderate magnetic conductivity, where interactions with the electric energy reservoir may unveil novel insights, could prove to be an intriguing avenue of research.

6   Conclusions & Outlook

Even in the absence of cosmological expansion, it was observed that the transition to conductivity involves oscillatory exchanges between electric and magnetic energies. Notably, it is the electric energy reservoir that primarily contributes to the kinetic and thermal energy reservoirs, as opposed to the direct involvement of magnetic energy, as observed in magnetohydrodynamics. Additionally, the duration of this transition plays a crucial role in causing a decrease in magnetic energy, with the extent of the drop depending on magnetic field strength and the Alfvén speed. The drop becomes smaller when the Alfvén speed approaches the speed of light. For shorter transitions, electric energy is mostly converted into thermal energy. However, for longer transitions, there is an approximately equal exchange between electric and magnetic energies, with both contributing to thermalization.

While the present simulations have still not been able to explore the regime of a turbulent transition into the radiation-dominated era, they have revealed a great wealth of detail even just for the one-dimensional case. These simulations therefore provide an important benchmark for future models. In particular, the identification of the Q_{G} term providing the energy input in magnetogenesis from reheating may have been overlooked in the past. It demonstrated, for example, that the original idea of producing a growing magnetic field for positive exponents in the relation between f and the scale factor cannot lead to a net electric energy gain. This is because previous work focused mostly of the scaled vector potential, $\boldsymbol{\mathcal{A}} = f\boldsymbol{A}$, which can grow even if $|\boldsymbol{A}|$ stays constant. Clarifying this further would therefore be another import objective for future work.

References

Adshead, Peter, Giblin, John T., Pieroni, Mauro, and Weiner, Zachary J. (Apr. 2020). "Constraining axion inflation with gravitational waves from preheating". In: *Physical Review D* 101.8. DOI: 10.1103/physrevd.101.083534. URL: https://doi.org/10.1103%2Fphysrevd.101.083534.

Adshead, Peter, Giblin, John T., Scully, Timothy R., and Sfakianakis, Evangelos I. (Oct. 2016). "Magnetogenesis from axion inflation". In: *Journal of Cosmology and Astroparticle Physics* 2016.10, pp. 039–039. DOI: 10.1088/1475-7516/2016/10/039. URL: https://doi.org/10.1088%2F1475-7516%2F2016%2F10%2F039.

Adshead, Peter, Jr., John T. Giblin, Scully, Timothy R., and Sfakianakis, Evangelos I. (Dec. 2015). "Gauge-preheating and the end of axion inflation". In: *Journal of Cosmology and Astroparticle Physics* 2015.12, pp. 034–034. DOI: 10.1088/1475-7516/2015/12/034. URL: https://doi.org/10.1088%2F1475-7516%2F2015%2F12%2F034.

Ahmed, Aqeel, Grzadkowski, Bohdan, and Socha, Anna (2022). "Implications of time-dependent inflaton decay on reheating and dark matter production". In: *Physics Letters B* 831, p. 137201. ISSN: 0370-2693. DOI: https://doi.org/10.1016/j.physletb.2022.137201. URL: https://www.sciencedirect.com/science/article/pii/S0370269322003355.

Alfvén, Hannes (Oct. 1942). "Existence of Electromagnetic-Hydrodynamic Waves". In: *Nature* 150.3805, pp. 405–406. ISSN: 0028-0836. DOI: 10.1038/150405a0. URL: http://www.nature.com/doifinder/10.1038/150405a0.

Batista, Rafael Alves, Saveliev, Andrey, and Gouveia Dal Pino, Elisabete M de (Sept. 2019). "The Impact of Plasma Instabilities on the Spectra of TeV Blazars". In: *Monthly Notices of the Royal Astronomical Society.* DOI: 10.1093/mnras/stz2389. URL: https://doi.org/10.1093%2Fmnras%2Fstz2389.

Brandenburg, A., Jennings, R. L., et al. (1996). "Magnetic structures in a dynamo simulation". In: *Journal of Fluid Mechanics* 306, pp. 325–352. DOI: 10.1017/S0022112096001322.

Brandenburg, Axel, He, Yutong, and Sharma, Ramkishor (Nov. 2021). "Simulations of Helical Inflationary Magnetogenesis and Gravitational Waves". In: *The Astrophysical Journal* 922.2, p. 192. DOI: 10.3847/1538-4357/ac20d9. URL: https://doi.org/10.3847%2F1538-4357%2Fac20d9.

Brandenburg, Axel, Nordlund, Ake, Stein, Robert F., and Torkelsson, Ulf (June 1995). "Dynamo-generated Turbulence and Large-Scale Magnetic Fields in a Keplerian Shear Flow". In: *Astrophys. J.* 446, p. 741. DOI: 10.1086/175831.

Brandenburg, Axel and Ntormousi, Evangelia (2021). "Dynamo effect in unstirred self-gravitating turbulence". In: *Monthly Notices of the Royal Astronomical Society.* URL: https://api.semanticscholar.org/CorpusID:244921124.

Brandenburg, Axel and Protiti, Nousaba Nasrin (Aug. 2023). "Electromagnetic Conversion into Kinetic and Thermal Energies". In: *Entropy* 25.9, p. 1270. DOI: 10.3390/e25091270. URL: https://doi.org/10.3390%2Fe25091270.

Brandenburg, Axel and Sharma, Ramkishor (Oct. 2021). "Simulating Relic Gravitational Waves from Inflationary Magnetogenesis". In: *Astrophys. J.* 920.1, 26, p. 26. DOI: 10.3847/1538-4357/ac1599. arXiv: 2106.03857 [astro-ph.CO].

Broderick, Avery E., Chang, Philip, and Pfrommer, Christoph (May 2012). "The cosmological impact of luminous TeV blazars. i. implications of plasma instabilities for the intergalactic magnetic field and extragalactic gamma-ray background". In: *The Astrophysical Journal* 752.1, p. 22. DOI: 10.1088/0004-637x/752/1/22. URL: https://doi.org/10.1088%2F0004-637x%2F752%2F1%2F22.

Broderick, Avery E., Tiede, Paul, et al. (Nov. 2018). "Missing Gamma-Ray Halos and the Need for New Physics in the Gamma-Ray Sky". In: *The Astrophysical Journal* 868.2, p. 87. DOI: 10.3847/1538-4357/aae5f2. URL: https://doi.org/10.3847%2F1538-4357%2Faae5f2.

Collaboration, The et al. (Feb. 2021). "The Pencil Code, a modular MPI code for partial differential equations and particles: multipurpose and multiuser-maintained". In: *Journal of Open Source Software* 6.58, p. 2807. DOI: 10.21105/joss.02807. URL: https://doi.org/10.21105%2Fjoss.02807.

Davidson, P. A. (2016). *Introduction to Magnetohydrodynamics*. 2nd ed. Cambridge Texts in Applied Mathematics. Cambridge University Press. DOI: 10.1017/9781316672853.

Demozzi, Vittoria, Mukhanov, Viatcheslav, and Rubinstein, Hector (Aug. 2009). "Magnetic fields from inflation?" In: *Journal of Cosmology and Astroparticle Physics* 2009.08, pp. 025–025. DOI: 10.1088/1475-7516/2009/08/025. URL: https://doi.org/10.1088%2F1475-7516%2F2009%2F08%2F025.

Durrer, Ruth and Neronov, Andrii (June 2013). "Cosmological magnetic fields: their generation, evolution and observation". In: *The Astronomy and Astrophysics Review* 21.1. DOI: 10.1007/s00159-013-0062-7. URL: https://doi.org/10.1007%2Fs00159-013-0062-7.

Ferreira, Ricardo J.Z, Jain, Rajeev Kumar, and Sloth, Martin S (Oct. 2013). "Inflationary magnetogenesis without the strong coupling problem". In: *Journal of Cosmology and Astroparticle Physics* 2013.10, pp. 004–004. DOI: 10.1088/1475-7516/2013/10/004. URL: https://doi.org/10.1088%2F1475-7516%2F2013%2F10%2F004.

He, Yutong, Roper Pol, Alberto, and Brandenburg, Axel (June 2023). "Modified propagation of gravitational waves from the early radiation era". In: *J. Cosmol. Astropart. Phys.* 2023.6, 025, p. 025. DOI: 10.1088/1475-7516/2023/06/025. arXiv: 2212.06082 [gr-qc].

Kobayashi, Takeshi and Afshordi, Niayesh (Oct. 2014). "Schwinger effect in 4D de Sitter space and constraints on magnetogenesis in the early universe". In: *Journal of High Energy Physics* 2014.10. DOI: 10.1007/jhep10(2014)166. URL: https://doi.org/10.1007%2Fjhep10%282014%29166.

Kobayashi, Takeshi and Sloth, Martin S. (July 2019). "Early cosmological evolution of primordial electromagnetic fields". In: *Physical Review D* 100.2. DOI: 10.1103/physrevd.100.023524. URL: https://doi.org/10.1103%2Fphysrevd.100.023524.

Kofman, Lev, Linde, Andrei, and Starobinsky, Alexei A. (Dec. 1994). "Reheating after Inflation". In: *Physical Review Letters* 73.24, pp. 3195–3198. DOI: 10.1103/physrevlett.73.3195. URL: https://doi.org/10.1103%2Fphysrevlett.73.3195.

Mukhanov, V. F., Feldman, H. A., and Brandenberger, R. H. (June 1992). "Theory of cosmological perturbations". In: *Phys. Rep.* 215.5-6, pp. 203–333. DOI: 10.1016/0370-1573(92)90044-Z.

Neronov, Andrii and Vovk, Ievgen (Apr. 2010). "Evidence for Strong Extragalactic Magnetic Fields from Fermi Observations of TeV Blazars". In: *Science* 328.5974, pp. 73–75. DOI: 10.1126/science.1184192. URL: https://doi.org/10.1126%2Fscience.1184192.

Ratra, Bharat (May 1992). "Cosmological "Seed" Magnetic Field from Inflation". In: *Astrophys. J. Lett.* 391, p. L1. DOI: 10.1086/186384.

Sharma, Ramkishor, Jagannathan, Sandhya, Seshadri, T. R., and Subramanian, Kandaswamy (Oct. 2017). "Challenges in inflationary magnetogenesis: Constraints from strong coupling, backreaction, and the Schwinger effect". In: *Physical Review D* 96.8. DOI: 10.1103/physrevd.96.083511. URL: https://doi.org/10.1103%2Fphysrevd.96.083511.

Sharma, Ramkishor, Subramanian, Kandaswamy, and Seshadri, T. R. (Apr. 2018). "Generation of helical magnetic field in a viable scenario of inflationary magnetogenesis". In: *Physical Review D* 97.8. DOI: 10.1103/physrevd.97.083503. URL: https://doi.org/10.1103%2Fphysrevd.97.083503.

Sironi, Lorenzo and Giannios, Dimitrios (May 2014). "Relativistic pair beams from TeV blazars: a source of reprocessed gEv emission rather than intergalactic heating". In: *The Astrophysical Journal* 787.1, p. 49. DOI: 10.1088/0004-637x/787/1/49. URL: https://doi.org/10.1088%2F0004-637x%2F787%2F1%2F49.

Subramanian, K. (Jan. 2010). "Magnetic fields in the early Universe". In: *Astronomische Nachrichten* 331.1, pp. 110–120. DOI: 10.1002/asna.200911312. URL: https://doi.org/10.1002%2Fasna.200911312.

Subramanian, Kandaswamy (May 2016). "The origin, evolution and signatures of primordial magnetic fields". In: *Reports on Progress in Physics* 79.7, p. 076901. DOI: 10.1088/0034-4885/79/7/076901. URL: https://doi.org/10.1088%2F0034-4885%2F79%2F7%2F076901.

Taylor, A. M., Vovk, I., and Neronov, A. (Apr. 2011). "Extragalactic magnetic fields constraints from simultaneous GeV–TeV observations of blazars". In: *Astron. & Astrophys.* 529, A144. DOI: 10.1051/0004-6361/201116441. URL: https://doi.org/10.1051%2F0004-6361%2F201116441.